IONIZATION OF THE HYDROGEN MOLECULAR ION BY STRONG INFRARED LASER FIELDS

TSOGBAYAR TSEDNEE

A DISSERTATION SUBMITTED TO THE FACULTY OF GRADUATE STUDIES
IN PARTIAL FULFILMENT OF THE REQUIREMENTS
FOR THE DEGREE OF

DOCTOR OF PHILOSOPHY

GRADUATE PROGRAM IN PHYSICS AND ASTRONOMY
YORK UNIVERSITY
TORONTO, ONTARIO
MAY 2014

Abstract

The ionization of simple molecular targets, such as molecular hydrogen, or even the molecular hydrogen ion (H_2^+) by strong laser fields has become the focus of experimental research in the past few decades. On the theoretical side the problem presents two challenges: on the one hand one has to solve the problem numerically even in the one-electron case (H_2^+), since no analytic closed-form solution is possible; on the other hand there is the many-electron problem (H_2 and other diatomic molecules, such as N_2, O_2, etc.), which currently is at the limit of computational feasibility (H_2), or exceeds it for molecules with more than two electrons.

In this thesis the single-electron problem of the hydrogen molecular ion in intense continuous-wave laser fields is addressed. The focus is on ionization rates of the molecule as a function of internuclear separation within the framework that the motion of the nuclei can be neglected (Born-Oppenheimer approximation). First, the problem of the DC limit is considered, i.e., a strong static electric field is applied along the internuclear axis. The field ionization rate is calculated by

solving a stationary non-hermitean Schrödinger equation in a suitable coordinate system (prolate spheroidal coordinates). Some previously obtained values from the literature are reproduced; for larger internuclear separations improved values are obtained.

For the more interesting case of an infrared (continuous-wave) laser field Floquet theory is applied to transform the time-dependent Schrödinger equation for the electronic motion into a non-hermitean coupled-channel stationary problem. Ionization rates are found as a function of laser frequency (ω), and the low-frequency limit is pursued to understand how one can establish a connection to the DC limit. Results are obtained for the two lowest electronic states, which are named the *gerade* and *ungerade* (or even and odd) ground states in the field-free limit.

From the calculated results it is observed that the ionization rates peak at certain internuclear separations, such that a dissociating H_2^+ molecule will be preferentially field ionized. In addition, the thesis reports on calculations of so-called high harmonic generation - a process where photo-electrons acquire energy from the laser field, are deflected back by the linearly polarized laser and recombine under the emission of photons with energies that correspond to odd-integer multiples of the laser photon energy.

Dedication

To my father Tsednee Sanjjav and mother Adilbish Danaajav and my son Erdemtugs Tsogbayar

Acknowledgements

First of all, I would like to express my sincere gratefulness and respect to my supervisor, Professor Marko Horbatsch for his excellent guidance and advice, and in particular for his encouragements and suggestions. I sincerely appreciate his trust that had brought me to study at York University from overseas, my country, Mongolia. I would also like to thank him for the honest criticisms and willingness to spend the time to properly explain things to me.

I thank Professor Tom Kirchner for all advice and all the letters of recommendation allowing me to get an Ontario Graduate Scholarship and my postdoctoral research work.

I want to thank graduate students in the group of AMO physics and in particular, PhD student Alain Marsman for all the help and a willingness to spend the time to explain whatever I asked.

I would like to thank the York Physics and Astronomy departmental staff for providing me with all the help and assistance I needed, and especially, to Marlene

and Lauren for making everything simple enough.

I would like to thank people to whom I met before I came to York University. I am deeply thankful to Academician, Professor Kh. Namsrai for his valuable guidance and encouragement. I want to thank Academicians Ts. Baatar, R. Togoo and Professors D. Nyamaa, D. Naidan from the Institute of Physics & Technology, Mongolian Academy of Sciences, and Professors O. Lkhagva, Ts. Gantsog, S. Davaa, D. Sangaa and S. Chuluuntsetseg (staff member) at the National University of Mongolia.

I would also like to thank Dr. V. I. Korobov for directing my research in the Bogoliubov Laboratory of Theoretical Physics, Joint Institute for Nuclear Researches in Dubna, Russia.

I would like to thank D. Narandorj (my uncle), L. Gerelchimeg, B. Myagmarsuren and L. Borkhuu and other teachers in a secondary school, Chandmani soum, Khovd province.

My deepest gratitude goes to my father S. Tsednee and my mother D. Adilbish for their warm love and support in my life and my older brother Ts. Altaisaikhan and younger brother and sisters, and other relatives for their encouragement.

Finally, I want to thank Professor P. Garrett and PhD student J. Badamsambuu at the University of Guelph and Dr. G. Sodnomdorj, P. Erdenebileg, Z. Gantulga and others for their encouragement in Toronto.

Table of Contents

List of Tables

List of Figures

1 Theoretical methods

1.1 Introduction

Over the past few decades the ionization dynamics of the hydrogen molecular ion in an intense laser field has attracted much interest, because this fundamental system shows many interesting phenomena, such as, vibrational trapping, bond softening (hardening), above-threshold dissociation, and enhancement of the ionization rates as a function of internuclear separation R for the lowest two states while it is exposed to an external electric field [1-9].

In this thesis we will consider theoretical studies of the enhancement of the ionization rates as a function of R for the lowest two states of the ion in DC and AC electric fields. Theoretical studies of this phenomenon were started by Bandrauk and his cowokers [10], and later were continued by Shakeshaft *et al* [11], Plummer and Madsen [12], and Chu and Chu [13]. Experimental data were obtained in [5, 9].

The main purpose of this thesis is to investigate the DC and AC Stark resonance parameters for the lowest two states of the ion using a pseudospectral method

combined with a complex absorbing potential, and to obtain more accurate values of the resonance energies and widths (decay rates), and to explain the enhancement using the obtained results. Furthermore, it is shown how the ionization rates as a function of internuclear separation R in the case of a low-frequency laser field is related to those obtained in the DC limit. Finally, high harmonic generation spectra for the states are obtained using the Floquet wave function and an understating of how the enhancement of the ionization rate at certain internuclear separations can affect the harmonic generation rate is investigated.

In this chapter we introduce the theoretical methods which are used in the calculations. Sect. 1.2 presents the concept of Siegert states and its connection to the tunneling resonance phenomenon for atomic hydrogen and the hydrogen molecular ion in a DC and AC electric fields. A complex absorbing potential method that is used to solve the resonance problem is discussed in Sect.1.2, as well. The Floquet theory for the AC case is explained in Sect. 1.3. In Sect. 1.4 a pseudospectral representation is introduced by which the Schrödinger equation is solved in cylindrical and prolate spheroidal coordinates. Sect 1.5 presents a summary. In this thesis atomic units ($\hbar = m_c = e = 1$) are used in the calculation.

1.2 Siegert states and complex absorbing potential

1.2.1 The tunneling resonance phenomenon

Resonance phenomena are common in various fields of atomic, molecular and chemical physics, such as, in electron-atom scattering, photoionization, and autoionization, to name a few. In this thesis we study theoretically the following resonance phenomena: resonant tunneling ionization of the H_2^+ ion a DC electric field, as well as the over-the-barrier and multiphoton mechanisms for the molecular ion in intense low-frequency fields.

For the H_2^+ ion, in the presence of an external (DC) electric field, the originally symmetric Coulomb two-center potential experienced by the electron is distorted: the outer edge of one well is raised, while the outer edge of the other well is lowered, and the reflection symmetry of the electronic potential is lost. The lowest gerade and ungerade states of the ion (which are nearly degenerate at large R in the absence of the field) are strongly split: the lower state remains in the deeper well, and the other 'upper' state is localized in the upper well. While the electron in the deeper well can tunnel through the lower barrier, the electron which sits in the higher well can be ionized by tunneling through the middle barrier or by escape over the barrier (Figure 1.1).

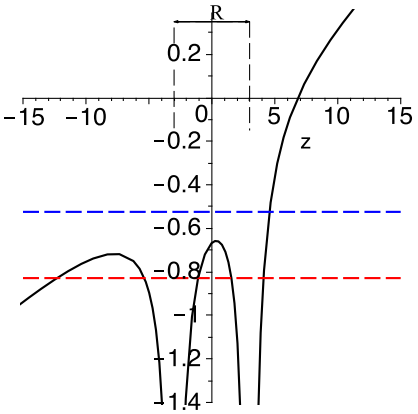

Figure 1.1: The Coulomb potential of the H_2^+ ion at separation $R = 6\,au$ distorted by an electric field of strength $F = 0.0533\,au$, which is along the z-axis. The dashed lines indicate the real parts of the quasienergy for the lower (red) and upper (blue) states. The graph shows a cut along the internuclear axis.

Resonance states can be described by the complex eigenenergy (quasienergy):

$$E_{res} = E_R - i\Gamma/2. \tag{1.1}$$

Here the real part E_R is the resonance position, and Γ is the resonance width, or the full width at half maximum which is related the ionization rate. Thus the natural decay time $\tau = 1/\Gamma$ of the resonance state follows Refs.[14, 15].

Note that the decay time or ionization rate is a concept within a time-dependent approach: in the DC tunneling problem τ represents the time when an initially fully populated quasi-static state reaches a population of e^{-1}, ($|\psi(\tau)|^2 = |\psi(0)|^2 e^{-\Gamma\tau} => e^{-1}$). The resonance width Γ is associated with a scattering problem: scattering

of photons with energy E from the potential of two protons separated by R as well as the external field results in a Breit-Wigner profile centered at $E = E_R$ with width Γ, which is superimposed on a slowly varying background scattering cross section $\sigma_{bg}(E)$. The non-Hermitean eigenvalue approach provides a link to the quasi-stationary time-dependent decay problem as explained in subsection (1.2.2).

1.2.2 Siegert state

The tunneling resonance phenomenon discussed in Section 1.2.1 is closely related to the problem of scattering of an electron off a (spherical) potential, since the scattering cross section (1.2) shows a characteristic peak near the resonance energy $E_R = \Re(E_{res})$, which can be described by the so-called Lorentz or Breit-Wigner formula:

$$\sigma_{res}(E) = \frac{1}{2\pi} \frac{\Gamma}{[(E - E_R)^2] + (\Gamma/2)^2}. \tag{1.2}$$

where the width characterizes the decay property of the resonance state $\Gamma = -2\Im(E_{res})$ [16].

This tunneling (decaying) resonance state is referred to as a Siegert [17] state, for which the wave function is described only by the outgoing component of the resonance wave function. This outgoing wave function is not in the Hilbert space of square-integrable functions, and diverges at the complex resonance eigenvalue (cf. Eq.(1.8) below).

For the sake of simplicity, now consider within stationary scattering theory a one-dimensional resonance (scattering) problem, such that, the radial Hamiltonian with a short-range potential $V(r)$ which supports resonances, defined on $r \in [0, \infty)$, vanishing for $r > r_0$ has the form

$$H = -\frac{1}{2}\frac{d^2}{dr^2} + V(r). \tag{1.3}$$

One model potential shown in Fig. 1.2a is

$$V(r) = Cr^2 e^{-\lambda r}, \text{ with } \lambda > 0. \tag{1.4}$$

Depending on the choice of C and λ it allows for one or more resonant states at $E > 0$ (for details cf [18]). It has no truly bound states (Fig. 1.2a).

Another model potential

$$V(r) = \begin{cases} -V_0, & \text{for } 0 \leq r < a, \\ V_0, & \text{for } a \leq r < 2a, \\ 0, & \text{for } r \geq 2a \end{cases} \tag{1.5}$$

(Fig. 1.2b) for the choice $a = 1, V_0 = 10$ (atomic units) is shown to have one true bound state and one quasi-bound resonant state. These properties were discussed by Santra *et al* [19].

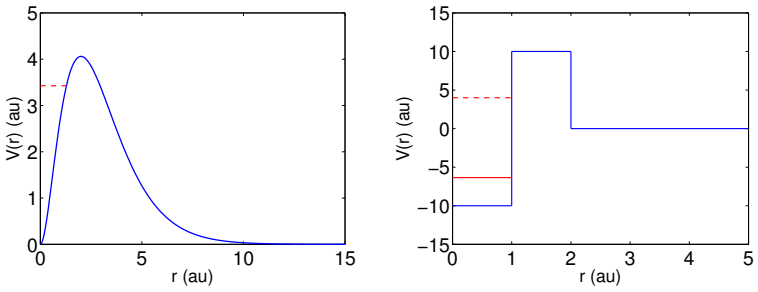

(a) (b)

Figure 1.2: Model potentials: (a) Eq.(1.4) with $C = 7.5$ and $\lambda = 1$; (b) Eq.(1.5) with $V_0 = 10$ and $a = 1$. The dashed (a, b) and the solid (b) lines indicate the position of the first resonance state and the bound state respectively. These values are obtained from for (a) in Ref.[18] and for (b) in Ref.[19].

According to the Siegert method [17], the radial resonance wave function, which vanishes at the origin, has the following asymptotic ($r > r_0$) behaviour:

$$u(r) \sim e^{ikr} \text{ for } r \to \infty, \tag{1.6}$$

with the momentum $k = (2E_{res})^{1/2}$. To obtain the Siegert resonance energy one needs to use the Siegert boundary condition (logarithmic derivative condition) at $r = r_0$, such that

$$\frac{d}{dr}u(r)|_{r=r_0} = iku(r_0). \tag{1.7}$$

For complex momentum k, one can use $k = |k|e^{-i\beta}$, and $\beta = \frac{1}{2}\arg(E_{res})$. Then

equation (1.6) becomes

$$u(r) \sim e^{i|k|re^{-i\beta}} = e^{i|k|r\cos\beta}e^{|k|r\sin\beta}. \tag{1.8}$$

From the second exponential in equation (1.8) it is now obvious that the outgoing wave function (1.6) diverges at the complex resonance energy E_{res}. Because of this asymptotic divergence, it is difficult to solve the resonance problem in this way. Alternative methods which do not involve the complications of continuum wave functions or explicit scattering calculations have been developed and implemented, in which one can directly calculate the complex energy of the resonance state.

1.2.3 Method of Complex Scaling

The first known approach in this class is the method of complex scaling (CS) or complex rotation CR developed by Reinhardt and coworkers [20, 21] and [22, 23, 24, 25, 26, 27, 28, 29, 30]. In the CS method the complex scaling transformation of the particle coordinate

$$r \to re^{i\theta} \tag{1.9}$$

is applied, where θ is called the rotation angle, which is real and positive. Under this transformation, the spectrum of the rotated (complex scaled) Hamiltonian is transformed in the following way: (i) the bound states on the negative real axis of the complex E_{res} plane are invariant; (ii) the cuts representing the $E > 0$ continuum

rotate downward with an angle of 2θ with respect to the real axis $\Re(E_{res})$, and thus unveil the resonance poles when θ is larger than β. Figure 1.3 shows the spectrum in the complex energy plane for a fixed value of θ. As the parameter θ is increased from zero, the resonance states which are defined by θ-trajectories in the complex E_{res} plane remain relatively stable within a certain range of θ values. The best approximated value of the resonance energy is obtained by looking for stability of the complex resonance energy along the θ-trajectory.

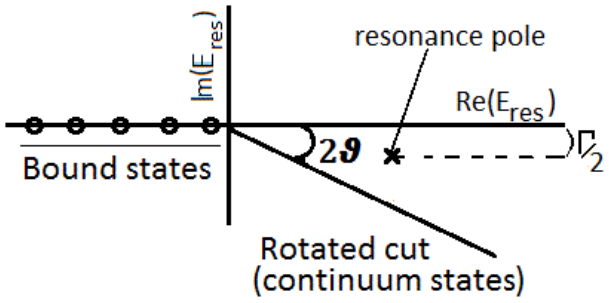

Figure 1.3: The bound-state energies are invariant; as the continuum energies rotate when θ is varied, the complex resonance eigenvalue ($\times$) is exposed. In this figure an arbitrary choice was made (location of 5 bound states and one resonant state).

With the transformation (1.9), the asymptotically diverging resonance wave (1.6) becomes

$$u(r) \sim e^{i|k|e^{-i\beta}|r|e^{i\theta}} = e^{i|k||r|e^{i(\theta-\beta)}} = e^{i|k||r|\cos(\theta-\beta)} e^{-|k||r|\sin(\theta-\beta)} \tag{1.10}$$

which is asymptotically convergent, that is, square integrable (L^2) for $\pi/2 > (\theta -$

$\beta) > 0$. Thus the CS or CR method allows the conclusion that the resonance parameters (both resonance position and width) can be obtained using bound-state type wave functions (or so called L^2 wave functions). This is true provided the CR parameter θ is sufficiently large compared to the resonance width, i.e., that the resonance pole is isolated from the continuum (Fig.1.3). This means that now the resonance state is a quasi-bound state embedded in the continuum.

In this thesis, we employ this method for the Stark resonance problem for the hydrogen molecular ion in an external electric field. A closely related approach to CS that allows us to avoid the use of scattering wave functions is the complex absorbing potential (CAP) method, which will be discussed separately in the following subsection.

1.2.4 Complex absorbing potential

In this subsection we will discuss the CAP method, which we have employed to investigate the DC Stark resonance problem for atomic hydrogen and the hydrogen molecular ion, as well the AC Stark resonance problem for the H_2^+ ion. The CAPs were first used to calculate resonance parameters due to the quasi-bound character of the resonance state for a model potential by Jolicard and Austin [31]. Riss and Meyer [32] gave a detailed mathematical investigation on the implementation of the CAP method. The physical idea of the CAP method is to add a complex absorbing

potential to the resonance Hamiltonian, which is responsible for a damping of the outgoing wave in the asymptotic region, that is, making the Siegert states L^2-integrable. Then one only needs to calculate a complex eigenvalue problem to get the resonance parameters (resonance position E_R and width $\Gamma = -2\Im(E_{res})$). For the resonance Hamiltonian (1.3), we can add a complex absorbing term $-i\eta\, W$:

$$H(\eta) = H - i\eta W(r) \tag{1.11}$$

where η is a small positive parameter determining the CAP strength, and W is a positive (piecewise) potential function. The form of the W potential used in the thesis is

$$W(r) = \Theta(r - r_c)(r - r_c)^2, \tag{1.12}$$

where Θ is the Heaviside step-function and r_c determines the point where the absorber starts to dampen the outgoing resonance wave.

In analogy to the dependence on the parameter θ in the CS or CR method, as we vary the strength parameter η, thereby creating an η-trajectory in the complex plane, the complex eigenvalue E_{res} of a Siegert resonance state stabilizes in the complex plane. Note that stabilization is observed in the vicinity of some finite value $\eta \approx \eta_{stab}$.

However to obtain a true accurate resonance parameter E_{res} we should avoid this complex artifact, taking somehow a limit $\eta \to 0$. The first approach to achieve

this was given by Riss and Meyer [32]. They could show that: if there is an energy $E_0 \neq 0$ and a family of eigenvalues $E(\eta)$ such that

$$E(\eta) \to E_0 \text{ for } \eta \to 0 \tag{1.13}$$

then E_0 is either the energy of a bound state or of a Siegert resonance state of the (unperturbed) $H(\eta)$. Indeed, performing the limit $\eta \to 0$ is not meaningful within a fixed finite real basis set representation: the smaller the value of η, the larger the delocalization of the eigenfunctions $\psi(\eta)$, so they cannot be represented with a finite basis set if η becomes too small; a larger η is needed in order to spatially restrict the wave function.

However, Riss and Meyer developed an iterative correction scheme to determine an accurate Siegert eigenvalue from the CAP spectra at finite, somewhat larger η values. They proposed a Taylor expansion of $E(\eta)$ at any given η to remove η-dependence order by order. In order to minimize the "total error" $E_{fb}(\eta) - E_0$, as the difference between the complex energy eigenvalue $E_{fb} = E_{fb}(\eta)$ obtained with a finite basis and the exact value E_0, there must be an optimal value $\eta = \tilde{\eta}$.

One can remove the lowest-order terms of an expansion in $\tilde{\eta}$ by defining the nth order corrected energy as

$$E^{(n)} = E^{(n)}(\tilde{\eta}) = E_{fb}(\tilde{\eta}) + \sum_{j=1}^{n} \frac{(-\tilde{\eta})^j}{j!} \frac{d^j E_{fb}}{d\eta^j}\Big|_{\eta=\tilde{\eta}}, \tag{1.14}$$

The optimal value $\tilde{\eta}^{(n)}$ is found by

$$\Big|\frac{\eta^{n+1}}{(n+1)!}\frac{d^{n+1}E_{fb}}{d\eta^{n+1}}\Big|_{\eta=\tilde{\eta}} = \min, n = 0, 1, 2, \ldots \tag{1.15}$$

where the derivative is evaluated by finite differences along the η-trajectory.

The first derivative can be obtained by employing the generalized Hellman-Feynman theorem [33]

$$\frac{dE_{fb}}{d\eta} = -i\langle\psi(\eta)|W|\psi(\eta)\rangle\,. \tag{1.16}$$

The first-order corrected energy becomes

$$E^{(1)} = \langle\psi(\tilde{\eta})|H(\tilde{\eta})|\psi(\tilde{\eta})\rangle + (-\tilde{\eta})(-i\langle\psi(\tilde{\eta})|W|\psi(\tilde{\eta})\rangle) = \tag{1.17}$$

$$\langle\psi(\tilde{\eta})|H - i\tilde{\eta}W + i\tilde{\eta}W|\psi(\tilde{\eta})\rangle = \langle\psi(\tilde{\eta})|H|\psi(\tilde{\eta})\rangle. \tag{1.18}$$

This remarkable result states that we simply need the complex expectation value of the Hamiltonian H with respect to the eigenstate of the artificial Hamiltonian $H(\eta)$ evaluated for $\eta \approx \tilde{\eta}$ given by (1.15). To put it differently, the contribution of the CAP to the energy is removed to the first order by this perturbation theory. Indeed, the nth order correction can be recognized as the removal of the artificial CAP within nth order perturbation theory.

The trajectory $E_{fb}(\eta)$ itself thus contains the $(n = 0)$ RM results as an accumulation point. Similarly, for higher orders $n > 0$ one also obtains η-trajectories. For higher orders n the optimal values $\tilde{\eta}^{(n)}$ can be larger since the artifact of the CAP is removed 'more completely'.

The second approach to remove the artifact due to the CAP was given by Lefebvre, Sindelka and Moiseyev [34], in which the complex eigenvalue is obtained by using a Padé extrapolation, in the limit $E_{res}(\eta)_{\eta\to 0}$. This method is well discussed in [35], and was extended to calculate the Dirac-supercritical resonance problem in [36]. Following Eq.(5) in Ref.[36], (cf Ref.[34]) the Padé approximant for $E_{fb}(\eta)$ is obtained from

$$E_{Padé}(\eta) = \frac{\sum_{i=0}^{N_1} p_i \eta^i}{1 + \sum_{j=1}^{N_1+1} q_j \eta^j}, \tag{1.19}$$

where p_i and q_j are complex coefficients, and $N_p = 2(N_1+1)$ is the number of points used in the approximant. The $\eta = 0$ limit is given by p_0. In order to determine the Padé coefficients $\{p_i, q_j\}$ one selects a number of $E_{fb}(\eta_k), k = 1 \ldots N_p$ and solves a linear system of equations.

Although the Riss-Meyer iterative correction scheme or the Padé approximation enable us to remove the artifact from the CAP spectra and obtain an accurate Siegert resonance energy, the wave function still remains η-dependent. However, the most accurate resonance wave function is assumed to be $\psi(\tilde{\eta})$.

1.3 Floquet theory

For the case when the external field is a not static and provided by a laser we need to solve the time-dependent Schrödinger equation (TDSE). If a time-dependent

Hamiltonian is periodic in time, it is possible to make a certain general statement for the solution of the time-dependent Schrödinger equation. The theory for this system is known as Floquet theory [37].

Consider the TDSE in atomic units,

$$i\frac{\partial}{\partial t}\Psi(\mathbf{r},t) = H(\mathbf{r},t)\Psi(\mathbf{r},t) = [H_0 + V_L(\mathbf{r},t)]\Psi(\mathbf{r},t), \tag{1.20}$$

where the Hamiltonian is periodic in time with period $T = 2\pi/\omega$, that is, $H(\mathbf{r}, t + T) = H(\mathbf{r}, t)$, and H_0 is the unperturbed Hamiltonian and $V_L(\mathbf{r}, t)$ is an external (laser) electric field with frequency ω.

According to Floquet theory [37], the solution $\Psi_F^\alpha(\mathbf{r}, t)$ can be written in the form

$$\Psi_F^\alpha(\mathbf{r},t) = e^{-iE_F^\alpha t}\Phi_F^\alpha(\mathbf{r},t), \tag{1.21}$$

$$\Phi_F^\alpha(\mathbf{r},t+T) = \Phi_F^\alpha(\mathbf{r},t) = \sum_{n=-\infty}^{\infty} e^{in\omega t}\phi_n^\alpha(\mathbf{r}) \approx \sum_{-N_F/2}^{N_F/2} e^{in\omega t}\phi_n^\alpha(\mathbf{r}), \tag{1.22}$$

where E_F^α is called the Floquet quasi-energy, and the $\phi_n^\alpha(\mathbf{r})$ obey time-independent coupled-channel equations. The solution ansatz implies that the probability density for adjacent periods maintains its shape, but the amplitude may decay exponentially when $\Im(E_F^\alpha) < 0$, and when $\Im(E_F^\alpha) > 0$ the states are not square integrable.

Substituting the solution (1.21) into the Schrödinger equation (1.20) we obtain an eigen problem with eigenvalues that does not depend on time:

$$H_F(\mathbf{r},t)\Phi_F^\alpha(\mathbf{r},t) = E_F^\alpha\Phi_F^\alpha(\mathbf{r},t), \tag{1.23}$$

where the Floquet (*steady-state*) Hamiltonian $H_F(\mathbf{r}, t)$ is defined as

$$H_F(\mathbf{r}, t) = H(\mathbf{r}, t) - i\frac{\partial}{\partial t}. \tag{1.24}$$

Obviously H_F is analogous to the Hamiltonian for stationary states of the time-independent Schrödinger equation, that is, the time variable t is treated in analogy to a coordinate variable, and the Schrödinger equation (1.23) is solved as for the stationary states of the time-independent Schrödinger equation. Once we find $\Phi_F^\alpha(\mathbf{r}, t)$ from the *steady-state* Schrödinger equation (1.23), we obtain the solution $\Psi_F^\alpha(\mathbf{r}, t)$ to the time-dependent Schrödinger equation (1.20) via equation (1.21).

The Floquet eigenfunctions make up a complete set, and any solution to equation (1.20) can be expanded as

$$\Psi(\mathbf{r}, t) = \sum_\alpha c_\alpha \Psi_F^\alpha(\mathbf{r}, t), \tag{1.25}$$

where the coefficients c_α are independent of time.

It is convenient to define a composite Hilbert space in both position and time, $R \bigoplus T$ [38, 39]. The spatial part R is spanned by square-integrable functions on configuration space $\mathbf{r}$, while the temporal part T is spanned by the complete, orthonormal set of functions $e^{in\omega t}$, where $n = 0, \pm 1, \pm 2, \ldots$. Then the Floquet eigenstates, $\Phi_n^\alpha(\mathbf{r}, t)$, satisfy the orthonormality condition

$$\langle\langle \Phi_n^\alpha(\mathbf{r}, t) | \Phi_m^\beta(\mathbf{r}, t) \rangle\rangle \equiv \frac{1}{T}\int_0^T dt \int_{-\infty}^{\infty} \Phi_n^{\alpha *}(\mathbf{r}, t)\Phi_m^\beta(\mathbf{r}, t) d\mathbf{r} = \delta_{\alpha\beta}\delta_{nm}, \tag{1.26}$$

and form a complete set in $R \bigoplus T$:

$$\sum_{\alpha n} |\Phi_n^\alpha\rangle\rangle\langle\langle\Phi_n^\alpha| = \mathbf{1}. \tag{1.27}$$

We assume that the external field is provided by a linearly polarized monochromatic laser aligned with the internuclear axis of the diatomic molecule, and that the dipole approximation is valid. Then the interaction $V_L(\mathbf{r}, t)$ takes the form

$$V_L^{lg}(\mathbf{r}, t) = Fz \cos\omega t, \tag{1.28}$$

in length gauge, and

$$V_L^{vg}(\mathbf{r}, t) = i\frac{F}{\omega} \sin\omega t \frac{\partial}{\partial z} + \frac{F^2}{2\omega^2} \sin^2\omega t \tag{1.29}$$

in velocity gauge, where F is the laser field strength.

With the help of the definitions (1.26-1.27) for the Floquet eigenstates and equations (1.22-1.23), we obtain the time-independent coupled-channel matrix equations for ϕ_n^α in the composite Hilbert space $R \bigoplus T$

$$H_0\phi_n^\alpha(\mathbf{r}) + \frac{1}{2}Fz[\phi_{n-1}^\alpha(\mathbf{r}) + \phi_{n+1}^\alpha(\mathbf{r})] = (E_F - n\omega)\phi_n^\alpha(\mathbf{r}),$$
$$(n = 0, \pm1, \pm2 \ldots) \tag{1.30}$$

in length gauge, and

$$H_0\phi_n^\alpha(\mathbf{r}) + \frac{F^2}{2\omega^2}\Big[\frac{1}{4}\phi_{n-1}^\alpha(\mathbf{r}) - \frac{1}{2}\phi_n^\alpha(\mathbf{r}) + \frac{1}{4}\phi_{n+1}^\alpha(\mathbf{r})\Big] = (E_F - n\omega)\phi_n^\alpha(\mathbf{r}),$$
$$(n = 0, \pm1, \pm2 \ldots) \tag{1.31}$$

in velocity gauge, respectively.

1.4 Pseudospectral method

The name "spectral method" is given to a type of numerical approach for the solution of partial differential equations. In this approach the solution to the equation is approximated by a truncated series of special functions which are the eigenfunctions of some differential operator, often of Sturm-Liouville type. In contrast to the finite-difference method which is a local method, the spectral methods are global, in which computation is carried out at any point on the whole domain of computation, not only at discrete neighboring points.

In a pseudospectral method the computational domain is discretized with a prescribed quadrature for the integration measure. Basic descriptions of this method are: (i) an approximation of a function $u(x)$ is represented by a (Lagrange) interpolation polynomial, which is obtained using a discrete transform; (ii) once it is expressed by the global cardinal function the differentiation matrix of any order is obtained at any point of the interval.

In this thesis, we discuss two such methods in the following sections, since we use the Fourier-sine and Legendre spectral methods to solve the Schrödinger equation for the H atom and the H_2^+ ion, respectively. Other polynomial spectral methods are discussed in detail in [40-44].

1.4.1 Fourier (Sine) Spectral Method

In general, the solutions of partial differential equations can be expressed in terms of the Fourier series expansion. The full Fourier, cosine and sine series expansions in practice are written in terms of truncated sums. Employing these truncated Fourier series expansions leads to the Fourier Spectral Method to solve differential equations in a straightforward way and allows to obtain convergent results using relatively small basis sets because of the high-order approximation to derivatives as compared to finite differences. The pseudospectral Fourier grid method is based on the discrete Fourier transform, and it turns out that the truncated sum which arises in the calculation can be expressed in closed form based upon the global polynomial interpolant. The closed form, named the cardinal function for a given type of interpolation represents the cornerstone of this method, and its k-th derivative at the interpolation points produces the differentiation matrix.

The Fourier pseudospectral method is indeed preferable for a periodic problem, and has been first implemented in a quantum mechanics context by Meyer [45] and later by Marston [46]. For the sake of simplicity, now consider a one-dimensional truncated spectral representation $u_N(x)$ of the function $u(x)$ in interval $x \in [0, \pi]$, using the Fourier-sine series, which itself satisfies directly the physical boundary

condition

$$u_N(x) = \sum_{k=1}^{N} a_k \sin(kx). \tag{1.32}$$

The discrete Fourier sine series expansion coefficients a_k can be found by the trapezoidal rule:

$$a_k = \frac{2}{N+1} \sum_{i=1}^{N} u(x_i) \sin(kx_i),\ k = 1 \ldots N. \tag{1.33}$$

where x_i is a set of N equidistant grid points

$$x_i = \frac{\pi i}{N+1},\ i = 1 \ldots N. \tag{1.34}$$

Similarly, we obtain the inverse discrete Fourier transform, by inserting (1.33) into (1.32)

$$u_N(x) = \sum_{i=1}^{N} u(x_i) g_i(x). \tag{1.35}$$

This polynomial equation (1.35) interpolates the function $u(x)$ at the quadrature points of the trapezoidal formula. Here $g_i(x)$ is the Fourier-sine cardinal function

$$g_i(x) = \frac{2}{N+1} \sum_{k=1}^{N} \sin(kx_i) \sin(kx),\ x_i = \frac{\pi i}{N+1},\ i = 1 \ldots N. \tag{1.36}$$

The cardinal function $g_i(x)$ has the unique property

$$g_i(x_j) = \delta_{ij}. \tag{1.37}$$

This implies that the solution vector contains the desired solution evaluated at the grid points to the differential equation. In Figure 1.4a the cardinal functions $g_i(x)$ are shown for $N = 3$.

1.4.2 Polynomial (Legendre) Spectral Method

If the function $u(x)$ or any of its derivatives are not periodic, it is useful to use a non-periodic basis, such as a polynomial basis, usually based on the eigensolutions to some Sturm-Liouville problem. We will consider here only the discrete polynomial approximation of a function $u(x) \in L^2[a, b]$, where the interval $[a, b]$ can be bounded or unbounded.

The truncated expansion of any function $u(x) \in L^2[a = -1, b = 1]$ in real orthogonal polynomials $\varphi_k(x)$, which are complete in L^2_ω, is given as

$$u_N(x) = \sum_{k=0}^{N} \hat{u}_k \varphi_k(x), \tag{1.38}$$

where the discrete polynomial coefficients are obtained using a Gauss quadrature with weight $\omega_i(x)$, under which the polynomials are orthogonal,

$$\hat{u}_k = \frac{1}{\gamma_k} \sum_{i=0}^{N} u(x_i)\varphi_k(x_i)\omega_i. \tag{1.39}$$

Here γ_k is a normalization constant, found as

$$\gamma_k = \sum_{i=0}^{N} \varphi_k^2(x_i) w_i, \tag{1.40}$$

and x_i are non-equally spaced quadrature points, obtained as the $(N + 1)$ roots of the polynomials $\varphi_{N+1}(x)$ in general.

Inserting the discrete polyonomial transform (1.39) in the function expansion

(1.38), we have

$$u_N(x) = \sum_{i=0}^{N} u(x_i) l_i(x), \tag{1.41}$$

where the cardinal function $l_i(x)$, is obtained as the Christoffel-Darboux formula [44], and has the form

$$l_i(x) = \sum_{k=0}^{N} \frac{1}{\gamma_k} \varphi_k(x) \varphi_k(x_i) w_i. \tag{1.42}$$

Indeed, $l_i(x)$ is the Lagrange interpolation polynomial based on the Gaussian quadrature nodes, and again, (cf. (1.37)) has the unique property

$$l_i(x_j) = \delta_{ij}. \tag{1.43}$$

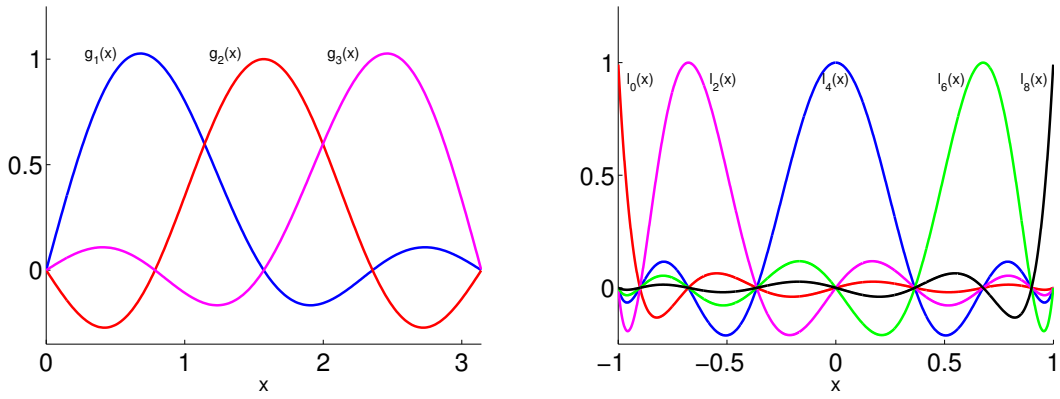

(a) (b)

Figure 1.4: Cardinal functions $g_j(x)$ (a), and $l_j(x)$ (b) with $N = 3$ and 8. These functions are used to interpolate the solution in between grid points.

In this calculation we restrict ourselves to one of the special cases of Jacobi

polynomials, the Legendre polynomial, $\varphi_k(x) = P_k(x)$, and the Legendre-Gauss-Lobatto grid points x_i, which are determined as the roots of the first derivative of the Legendre polynomial $P_N(x)$ with respect to x

$$P'_N(x_i) = 0, \quad i = 0, \ldots, N. \tag{1.44}$$

The pseudospectral representation of the truncated approximation of the function $u(x)$ can be written as

$$u_N(x) = \sum_{i=0}^{N} u(x_i) l_i(x), \tag{1.45}$$

where the cardinal function $l_i(x)$, is given in closed form

$$l_i(x) = \frac{-1}{N(N+1)} \frac{(1-x^2)}{(x-x_i)} \frac{P'_N(x)}{P_N(x_i)}. \tag{1.46}$$

In Figure 1.4b the cardinal functions $l_i(x)$ are shown for $N = 8$.

1.4.3 Coordinate system and mapping function

In this thesis we will use two different coordinate systems: cylindrical and prolate spheroidal. The former is applied to solve the resonance parameter problem for the H atom, while the latter is chosen for the resonance problem of the H_2^+ ion.

The cylindrical coordinates ρ, z and φ are related to the Cartesian coordinates x, y and z as follows,

$$x = \rho \cos\varphi, \; y = \rho \sin\varphi, \; z, \tag{1.47}$$

$$0 \leq \rho < \infty, \;\; -\infty < z < \infty, \;\; 0 \leq \varphi \leq 2\pi.$$

The transformations between prolate spheroidal coordinates $\{\mu, \nu, \varphi\}$ and the Cartesian coordinates $\{x, y, z\}$ are given as:

$$x = \frac{R}{2}\sqrt{(\mu^2-1)(1-\nu^2)}\cos\varphi,\ y = \frac{R}{2}\sqrt{(\mu^2-1)(1-\nu^2)}\sin\varphi,\ z = \frac{R}{2}\mu\nu, \quad (1.48)$$
$$1 \le \mu < \infty, \quad -1 \le \nu \le 1, \quad 0 \le \varphi \le 2\pi.$$

Before we implement the Fourier-sine and Legendre spectral methods we need to employ a mapping for the coordinates. A coordinate mapping is essential for spectral methods: it gives not only the opportunity to control the distribution of grid points, but also allows to play with the length of the chosen interval. For a Coulomb-type potential, expressing the interaction in atomic and molecular systems, the distribution of grid points near the singularity is controlled by a mapping function. We choose the following mapping functions for the ρ and z axes:

$$\rho(\theta_\rho) = L_\rho\frac{\theta_\rho}{\pi-\theta_\rho},\ z(\theta_z) = z_0 + L_z\tan(\theta_z/2),\ \ 0 \le \theta_\rho < \pi, \quad -\pi < \theta_z < \pi, \quad (1.49)$$

where L_ρ and L_z are the mapping range parameters. The plot of this mapping function is shown in Figure 1.5a. Different mappings for the ρ coordinate were also implemented in [47, 48, 49].

For the independent variables μ, ν in prolate spheroidal coordinate we map only the coordinate μ

$$\mu(x) = 1 + \frac{(1+x)}{2}(b-1), \quad (1.50)$$

where $x \in [-1, 1]$ and b is a mapping range parameter, which defines the size of the elliptic region in which the problem is solved, and we keep $\nu = y$, since $\nu \in [-1, 1]$. The grid structure for the mapping (1.50) is shown in Figure 1.5b. Comparing with Figure 1.4a, while we observe that the Fourier grid points are equidistant in the interval $[0, \pi]$, the Gauss-Legendre-Lobatto grid points are non-uniform, and more densely distributed to both ends of the interval $[-1, 1]$.

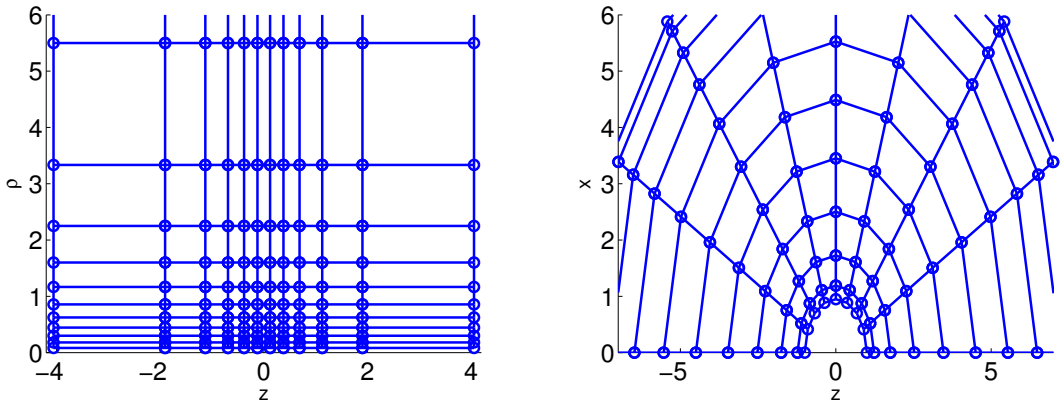

(a) (b)

Figure 1.5: Grid point distributions: cylindrical (a) and prolate spheroidal (b) coordinates. case (b): Small values of $N_\mu = 10, M_\nu = 8$ were chosen for clarity and $R = 2$. In practical calculations $N = 44, M = 12$.

1.4.4 Differentiation matrix based on the Fourier sine spectral method

Once we build an approximation of the function $u(x)$ in the chosen interval using the cardinal functions, we can obtain the derivative of $u(x)$ at point x_j by differentiating

the global polynomials $g_i(x)$:

$$\frac{d}{dx}u_N(x)\Big|_{x_j} = \sum_{i=1}^{N} u(x_i)\frac{d}{dx}g_i(x)\Big|_{x_j} = \sum_{i=1}^{N} d_{ij}^{(1)}u(x_i). \tag{1.51}$$

Using equation (1.36), the entries of the first- and second-order Fourier-sine differentiation matrix are given by

$$d_{ij}^{(1)} = \frac{2}{N+1}\sum_{k=1}^{N} k\,\sin(kx_i)\cos(kx_j), \tag{1.52}$$

$$d_{ij}^{(2)} = -\frac{2}{N+1}\sum_{k=1}^{N} k^2\,\sin(kx_i)\sin(kx_j).$$

1.4.5 Differentiation matrix based on the Legendre spectral method

By differentiating the global polynomial, $l_i(x)$ in the Lagrange interpolation polynomial (1.41) the derivative of the function $u(x)$ at the quadrature points can be evaluated as:

$$\frac{d}{dx}u_N(x)\Big|_{x_i} = \sum_{i=0}^{N} u(x_i)\frac{d}{dx}l_i(x)\Big|_{x_j} = \sum_{i=0}^{N} d_{ij}^{(1)}u(x_i). \tag{1.53}$$

The explicit form of the Legendre-Gauss-Lobatto differentiation matrix can be written as

$$d_{ij}^{(1)} = \frac{d}{dx}l_i(x)\Big|_{x_j} = \begin{cases} -\frac{N(N+1)}{4} & i = j = 0, \\ 0 & i = j \in [1,\ldots,N-1], \\ \frac{P_N(x_i)}{P_N(x_j)}\frac{1}{x_i - x_j} & i \neq j, \\ \frac{N(N+1)}{4} & i = j = N. \end{cases} \tag{1.54}$$

The higher-order derivatives can be easily obtained by $d_{ij}^{(n)} = \left(d_{ij}^{(1)}\right)^n$.

The transformations of derivatives for the mapping functions $\rho(\theta_\rho)$ and $\mu(x)$ are found as

$$\begin{aligned} \rho^{(n)}(\theta_\rho) = \frac{\partial^n \rho(\theta_\rho)}{\partial \theta_\rho^n}, \;\; \mu^{(n)}(x) = \frac{\partial^n \mu(x)}{\partial x^n}, \\ \frac{d^2}{d\rho^2} = \frac{\rho^{(1)}\partial_{\theta_\rho\theta_\rho} - \rho^{(2)}\partial_{\theta_\rho}}{[\rho^{(1)}(\theta_\rho)]^3}, \;\; \frac{d}{d\rho} = \frac{1}{\rho^{(1)}}\frac{\partial}{\partial\theta_\rho}, \\ \frac{d^2}{d\mu^2} = \frac{\mu^{(1)}\partial_{xx} - \mu^{(2)}\partial_x}{[\mu^{(1)}(x)]^3}, \;\; \frac{d}{d\mu} = \frac{1}{\mu^{(1)}}\frac{\partial}{\partial x}. \end{aligned} \tag{1.55}$$

The transformation of derivatives for the mapping function $z(\theta_z)$ is carried out in analogy to that for $\rho(\theta_\rho)$.

1.4.6 Discretization of the Schrödinger equation for atomic hydrogen in cylindrical coordinates

Consider first the time-independent eigenvalue problem for the Schrödinger equation in cylindrical coordinates for atomic hydrogen. Using the ansatz $\psi(\mathbf{r}) = u(\rho, z)e^{im\varphi}/\sqrt{\rho}$ to the Schrödinger equation, it has the form

$$\Big[-\frac{1}{2}\frac{d^2}{d\rho^2} + \frac{m^2 - 1/4}{2\rho^2} - \frac{1}{2}\frac{d^2}{dz^2} - \frac{1}{\sqrt{\rho^2 + z^2}}\Big]u(\rho, z) = Eu(\rho, z), \tag{1.56}$$

where $u(0, z) = u(\infty, z) = 0$, and m is the azimuthal quantum number. In this thesis only $m = 0$ is considered, since the field is assumed to be aligned with the z axis. In order to solve the 2D equation (1.56) we choose the following expansion in

analogy to equation (1.35)

$$u_{N_\rho M_z}(\rho, z) = \sum_{i=1}^{N_\rho} \sum_{j=1}^{M_z} u(\rho_i, z_j) g_i(\rho) g_j(z), \tag{1.57}$$

where the cardinal functions $g_i(\rho)$ and $g_j(z)$ are defined by equation (1.36):

$$g_i(\rho) = \frac{2}{N_\rho + 1} \sum_{k_\rho=1}^{N_\rho} \sin(k_\rho \theta_{\rho i}) \sin(k_\rho \theta_\rho), \tag{1.58}$$

$$g_j(z) = \frac{2}{M_z + 1} \sum_{k_z=1}^{M_z} \sin(k_\rho \theta_{zj}) \sin(k_\rho \theta_z).$$

Here N_ρ and M_z are the number of grid points along the ρ and z axes, respectively. With these Fourier-sine pseudospectral representations the eigenvalue problem (1.56) can be solved as:

$$\sum_{i'=1}^{N_\rho} \sum_{j'=1}^{M_z} \Big[-\frac{1}{2} T_{ij;i'j'} - \frac{1}{8\rho_i} \delta_{ii'} \delta_{jj'} - \frac{1}{\sqrt{\rho_i^2 + z_j^2}} \delta_{ii'} \delta_{jj'} \Big] u_{i'j'} = E\, \delta_{ii'} \delta_{jj'} u_{ij}, \tag{1.59}$$

where the kinetic energy operator is expressed as

$$T_{ij;i'j'} = \Big[T^{(\rho)}_{ii'} \delta_{jj'} + T^{(z)}_{jj'} \delta_{ii'} \Big]. \tag{1.60}$$

The components $T^{(\rho)}_{ii'}$ and $T^{(z)}_{jj'}$ have the forms

$$T^{(\rho)}_{ii'} = \frac{1}{[\rho^{(1)}(\theta_{\rho i})]^2} d^{(2)}_{ii'} - \frac{\rho^{(2)}(\theta_{\rho i})}{[\rho^{(1)}(\theta_{\rho i})]^3} d^{(1)}_{ii'} \tag{1.61}$$

$$T^{(z)}_{jj'} = \frac{1}{[z^{(1)}(\theta_{zj})]^2} d^{(2)}_{jj'} - \frac{z^{(2)}(\theta_{zj})}{[z^{(1)}(\theta_{zj})]^3} d^{(1)}_{jj'}, \tag{1.62}$$

where the first- and second-order differentiation matrices $d^{(1)}_{jj'}$ and $d^{(2)}_{ii'}$ are given by equation (1.52).

1.4.7 Discretization of the Schrödinger equation for the hydrogen molecular ion in prolate spheroidal coordinates

The field-free electronic Hamiltonian of the H_2^+ molecule can be written in atomic units as

$$H = -\frac{1}{2}\nabla_{\mathbf{r}}^2 - \frac{1}{|\mathbf{r} + \frac{R}{2}\mathbf{e}_z|} - \frac{1}{|\mathbf{r} - \frac{R}{2}\mathbf{e}_z|}, \tag{1.63}$$

where $\mathbf{r}$ is the electron position vector and R is the internuclear separation.

The kinetic energy operator and the Coulomb interaction become:

$$-\frac{1}{2}\nabla_{\mathbf{r}}^2 = -\frac{1}{2}\frac{4}{R^2(\mu^2-\nu^2)}\Big(\frac{\partial}{\partial\mu}[(\mu^2-1)\frac{\partial}{\partial\mu}] + \frac{\partial}{\partial\nu}[(1-\nu^2)\frac{\partial}{\partial\nu}] + \frac{\mu^2-\nu^2}{(\mu^2-1)(1-\nu^2)}\frac{\partial^2}{\partial\varphi^2}\Big), \tag{1.64}$$

$$V(\mu,\nu) = -\frac{4\mu}{R(\mu^2-\nu^2)}. \tag{1.65}$$

The wave function can now be expressed in separable form,

$$\Psi(\mu,\nu,\varphi) = \psi_m(\mu,\nu)e^{im\varphi}, \tag{1.66}$$

and separate eigenvalue problems for different $|m|$ values are obtained:

$$\begin{aligned} -\frac{1}{2}\frac{4}{R^2(\mu^2-\nu^2)}\Big[\frac{\partial}{\partial\mu}[(\mu^2-1)\frac{\partial}{\partial\mu}] + \frac{\partial}{\partial\nu}[(1-\nu^2)\frac{\partial}{\partial\nu}] - \\ \frac{m^2}{\mu^2-1} - \frac{m^2}{1-\nu^2}\Big]\psi_m - \frac{4\mu}{R(\mu^2-\nu^2)}\psi_m = E\psi_m. \end{aligned} \tag{1.67}$$

Because the solution for Eq.(1.67) is found analytically in terms of Legendre polynomials [50, 51, 52], it is natural to employ a Legendre-based pseudospectral

method. This follows since the zeroes of the Legendre polynomials are more densely distributed near $\nu = \pm 1$ [41, 44]. In this work we will only consider Σ electronic states ($|m| = 0$, no φ dependence), therefore, we will omit the subscript m from now on.

By extending the 1D expansion (1.45) to the 2D case we can approximate $\psi(\mu, \nu)$ by $\psi_{N_\mu, M_\nu}(\mu, \nu)$:

$$\psi(\mu, \nu) \approx \psi_{N_\mu, M_\nu}(\mu, \nu) = \sum_{i=0}^{N_\mu} \sum_{j=0}^{M_\nu} \phi(\mu_i, \nu_j) l_i[x(\mu)] l_j[y(\nu)]. \tag{1.68}$$

Both types of cardinal functions $l_i[x(\mu)]$ and $l_j[y(\nu)]$ are defined by equation (1.46)

$$l_i(x) = -\frac{1}{N_\mu(N_\mu + 1) P_{N_\mu}(x_i)} \frac{(1 - x^2) P'_{N_\mu}(x)}{x - x_i}, \tag{1.69}$$

$$l_j(y) = -\frac{1}{M_\nu(M_\nu + 1) P_{M_\nu}(y_j)} \frac{(1 - y^2) P'_{M_\nu}(y)}{y - y_j}. \tag{1.70}$$

They are needed at the grid points x_i and y_j, which are defined as the roots of equations

$$P'_{N_\mu}(x_i) = 0, \quad P'_{M_\nu}(y_j) = 0, \quad i = 0, \ldots, N_\mu, \;\; j = 0, \ldots, M_\nu. \tag{1.71}$$

After the transformation, the two-dimensional discretized eigenvalue problem (Eq.(1.67) to be satisfied exactly at grid points $\mu_{i'}, \nu_{j'}$) can be implemented directly:

$$\sum_{i'=0}^{N_\mu} \sum_{j'=0}^{M_\nu + 1} \Big[-\frac{1}{2} T_{ij;i'j'} - \frac{4}{R} \mu_i \delta_{ii'} \delta_{jj'} \Big] \phi_{i'j'} = E \, (\mu_i^2 - \nu_j^2) \delta_{ii'} \delta_{jj'} \phi_{ij}, \tag{1.72}$$

$$T_{ij;i'j'} = \frac{4}{R^2} \Big[T^{(\mu)}_{ii'} \delta_{jj'} + T^{(\nu)}_{jj'} \delta_{ii'} \Big]. \tag{1.73}$$

Here the partial matrices $T^{(\mu)}_{ii'}, T^{(\nu)}_{jj'}$ are related to the coordinates μ and ν, respectively, and are defined as follows:

$$T^{(\mu)}_{ii'} = (\mu_i^2 - 1)\frac{1}{[\mu_i^{(1)}]^2} d^{\mu}_{ii'} d^{\mu}_{ii'} + 2\mu_i \frac{1}{\mu_i^{(1)}} d^{\mu}_{ii'}, \tag{1.74}$$

$$T^{(\nu)}_{jj'} = (1 - \nu_j^2) d^{\nu}_{jj'} d^{\nu}_{jj'} - 2\nu_j d^{\nu}_{jj'}. \tag{1.75}$$

The matrices $d^{\mu}_{ii'}$ and $d^{\nu}_{jj'}$ are the first-order differentiation matrices using the Legendre Gauss-Lobatto points $x(\mu_i)$ and $y(\nu_j)$, and can be calculated by equation (1.54).

1.5 Summary

In this chapter we have set up a solution method for the tunneling resonance problem for atomic hydrogen and the hydrogen molecular ion in DC and AC electric fields. The complex absorbing potential method which enables us to avoid the use of continuum wave functions in resonance calculations is presented.

The Floquet method that permits us to find a solution for the time-dependent Schrödinger equation in terms of a matrix calculation is formulated for the AC Stark resonance problem in dipole approximation.

The mapped Fourier-sine and Legendre spectral methods are developed in detail. In this pseudospectral representation one needs to solve a matrix eigenvalue problem (cf. Eqs. (1.59, 1.72)) to obtain the solution of the Schrödinger equation and the

eigenvectors can give values of the wave function on chosen grid points. Then we can build the wave function not only on the chosen grid points, but also at arbitrary positions within the grid domain using the global Lagrange interpolation (cf. Eqs. (1.57, 1.68)). This is particularly useful when small grids are used and properties of the wave function are explored.

2 DC Stark resonance parameters for the hydrogen molecular ion in a static electric field

In this chapter we discuss the DC Stark resonance parameters for the H_2^+ ion in a static electric field using the theoretical methods described in chapter 1. We start with a brief discussion of previously accomplished research in this field in Sect. 2.1. The solution of the time-independent Schrödinger equation for the H_2^+ ion in cylindrical and prolate spheroidal coordinates is discussed in Sect. 2.2 and 2.3, respectively. In Sect. 2.4 we present the Stark-resonance Hamiltonian and the complex absorbing potential method. Sect. 2.5 contains the results for the Stark resonance parameters for the two lowest states of the ion. A summary follows in Sect. 2.6.

Originally published as Ts. Tsogbayar and M. Horbatsch, J. Phys. B: At. Mol. Opt. Phys. **46** 085004 (2013).

2.1 Introduction

The study of dissociative ionization of diatomic molecules in intense laser fields has been carried out both experimentally [1-9] and theoretically [10, 11, 12, 13, 53] following the pioneering theoretical work of L. V. Keldysh Ref.[54]. The simplest diatomic molecular ion H_2^+, is a prototype system which can be used to understand intense-field phenomena. For the first excited state (which in the field-free case has ungerade symmetry) the ionization rate as a function of internuclear separation R shows maxima at some critical separations beyond the equilibrium separation. This enhanced ionization at some larger internuclear separations has been observed experimentally [5, 9] and was discussed on the basis of numerical calculations [10]. In the case of low-frequency AC fields, and in the static (DC) field limit explanations were given for this phenomenon [10, 11, 12, 13].

Zuo and Bandrauk [10] observed that the over-the-barrier mechanism is the main reason for the peak in the ionization rate for the upper state as R is increased. Mulyukov *et al.*, [11] extended the argument using a somewhat different interpretation for this peak: their argument is based on the curves of the real and imaginary parts of the quasienergy for varying R, which is due to the mixing of the upper state with energetically nearby highly excited states that are localized in the lower well. Xi Chu and Shih-I Chu [13] argued that the charge-resonance effect and

multiphoton transitions to the excited electronic states represent the main mechanism responsible for the enhanced ionization phenomenon. In addition, Plummer and McCann [12] reasoned on the basis of localized electron density pictures of the upper resonance state that the critical distances validate a Coulomb explosion model [10, 55], while electron localization and simple over-the-barrier models of electron release are not appropriate mechanisms to explain this phenomenon. Bandrauk and Lu [56] have used time-dependent Schrödinger equation calculations to explore the DC Stark problem of H_2^+ in the presence of an additional magnetic field. Their reported findings and interpretations for the pure Stark problem are also precursors to the present work.

We carried out resonance calculations for the lower and upper states of H_2^+ in the static electric field which are obtained using the complex absorbing potential (CAP) method for varying internuclear distance R, to complement previous work [10, 11, 12, 13, 53]. To obtain more accurate values of the resonance parameters, the Riss-Meyer iterative method [32] and the Padé approximation and extrapolation to $\eta = 0$ [34, 35, 36] were implemented in analogy to the computationally more restricted work of Ref.[11]. We also obtain probability densities for both states to support the interpretation of why the ionization rate peaks at particular internuclear separations for two choices of strong-field parameters. The work is restricted to the case where the DC field is aligned with the internuclear axis. This restriction is not considered

to be severe, since the H_2^+ molecule will align prior to ionization [1, 57].

2.2 The hydrogen molecular ion in cylindrical coordinates

We initially attempted to solve the time-independent Schrödinger equation in cylindrical coordinates using the mapped Fourier sine grid method (MFSGM) discussed in Section 1.3.6. As a first test we worked on the Stark resonance problem for atomic hydrogen and results were published in [58]. For the H atom it was difficult to obtain convergence presumably due to the Coulomb singularity [49].

Following Eq.(1.56), the Schrödinger equation for the H_2^+ ion in cylindrical coordinates can be written as

$$\Big[-\frac{1}{2}\frac{d^2}{d\rho^2} + \frac{m^2-1/4}{2\rho^2} - \frac{1}{2}\frac{d^2}{dz^2} - V(\rho,z)\Big] u(\rho,z) = Eu(\rho,z). \tag{2.1}$$

The Coulomb potential energy $V(\rho,z)$ has the form

$$V(\rho,z) = -\frac{1}{\sqrt{\rho^2+(z-R/2)^2}} - \frac{1}{\sqrt{\rho^2+(z+R/2)^2}}. \tag{2.2}$$

The discretization of equation (2.1) can be carried out as discussed in Section 1.3.6. In Table 2.1 we show the eigenenergies for the ground $1s\sigma_g$ and first excited $2p\sigma_u$ states of the H_2^+ ion at $R = 2.0\,au$ while increasing the number of grid points N_ρ and M_z, along the coordinates ρ and z, respectively. This table shows that although the MFSGM can work for the H_2^+ ion, it gives slow convergence for the energy eigenvalue. Kosloff *et al* solved equation (2.1) using the Fourier-sine grid method,

but with a different mapping function for the ρ coordinate and obtained six-digits accurate energy value of $-1.10263\,au$ for the ground $1s\sigma_g$ state of the H_2^+ with a 16×16 mapped grid [47].

Table 2.1: Eigenenergies for the $1s\sigma_g$ and $2p\sigma_u$ states of the H_2^+ ion at an equilibrium distance $R = 2.0\,au$. The mapping parameters values are $L_\rho = 1$, $L_z = 1$ and $z_0 = 0$.

$N_\rho = M_z$	$E_{1s\sigma_g}\,(au)$	$E_{2p\sigma_u}\,(au)$
16	-1.1014	-0.6712
32	-1.1018	-0.6671
64	-1.1023	-0.6672
∞	-1.1026	-0.6675

Indeed the slow convergence of the energy eigenvalues for the two lowest states of H_2^+ shown in Table 2.1 implies that the MFSGM would not be the right choice to solve the Stark resonance problem for the ion because we need more digits of precision to get a well-converged value of the ionization rate. Therefore, we decided to make use of prolate spheroidal coordinates which were used by Xi Chu and S. I. Chu in Ref.[13].

2.3 The hydrogen molecular ion in prolate spheroidal coordinates

The two-dimensional discretized Schrödinger equation (1.59) for the H_2^+ ion can be solved directly. Our approach is very similar to that implemented in Ref.[13]. However, instead of using the variational symmetrized method we employ a direct collocation scheme here. The eigenvalues for low-lying Σ electronic states are obtained, and the eigenvectors give the values of the wave functions at chosen grid points $\{\mu_i, \nu_j\}$. Then we can interpolate the wave function on the whole computational domain using the computed eigenvectors and equation (1.68).

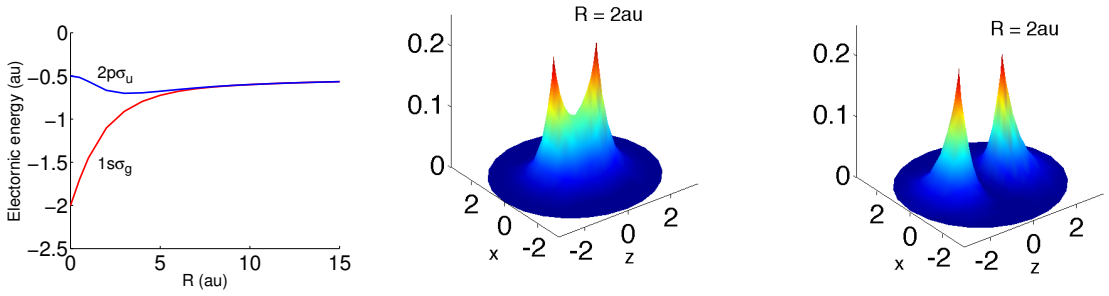

(a) (b) (c)

Figure 2.1: Electronic energy as a function of internuclear separation R for the lowest gerade (red) and ungerade (blue) states (a), and plots of $|\psi|^2$ for the $1s\sigma_g$ (b) and $2p\sigma_u$ (c) states for H_2^+ at $R = 2\,au$.

In Figure 2.1 we show some results for the ground and first excited states of

the ion. In panel (a) we show the electronic energy as a function of internuclear separation R for the gerade (red) and ungerade (blue) states of the ion. At large R the two states become nearly degenerate. Panels (b, c) demonstrate the probability density $|\psi|^2$ for the two states at the equilibrium distance $R = 2\,au$.

In Tables 2.2 and 2.3 we show the eigenenergy of the ground and first excited states and expectation values of the square of $r = (R/2)\sqrt{(\mu^2 + \nu^2 - 1)}$ (distance from the origin located between the two protons to the electron) and of the quadrupole moment $Q = (3z^2 - r^2)/2$ as a function of the grid parameters N_μ and M_ν at $R = 2.0\,au$. The collocation method gives rapidly converging results for moderate values of N_μ and M_ν.

Table 2.2: Some solutions for the $1s\sigma_g$ state of H_2^+ at $R = 2.0\,au$ for $a = 1, b = 20$.

N_μ	M_ν	$E_{1s\sigma_g}\,(au)$	$\langle r^2\rangle\,(au)$	$\langle Q\rangle\,(au)$
12	10	-1.102 363 088 395	2.394 521 797	0.469 280 805
24	10	-1.102 634 214 495	2.394 529 332	0.469 351 782
Exact [59]		-1.102 634 214 495	2.394 529 332	0.469 351 782

Table 2.3: The same as in Table 2.2, but for the $2p\sigma_u$ state of H_2^+.

N_μ	M_ν	$E_{2p\sigma_g}\,(au)$	$\langle r^2\rangle\,(au)$	$\langle Q\rangle\,(au)$
12	10	-0.667 581 425 111	4.808 027 665	2.306 704 155
24	10	-0.667 534 392 203	4.808 724 849	2.306 993 107
Exact [59]		-0.667 534 392 203	4.808 724 849	2.306 993 107

2.4 Stark-resonance Hamiltonian and complex absorbing potential method

The Stark Hamiltonian for the internuclear axis aligned with the field of strength F written in prolate spheroidal coordinates is given (in atomic units) as:

$$H_{res} = -\frac{1}{2}\nabla^2 - \frac{4\mu}{R(\mu^2-\nu^2)} + F\frac{R}{2}\mu\nu. \tag{2.3}$$

We add an artificial complex absorbing potential to this Hamiltonian to avoid the calculation of outgoing waves. One has to choose this complex absorbing potential only for the coordinate μ:

$$H = H_{res} - i\eta W = -\frac{1}{2}\nabla^2 - \frac{4\mu}{R(\mu^2-\nu^2)} + F\frac{R}{2}\mu\nu - i\eta W, \tag{2.4}$$
$$W(\mu) = \Theta(\mu-\mu_c)(\mu-\mu_c)^2.$$

Here Θ is the Heaviside step function, η is a small positive parameter, and μ_c determines the ellipse outside of which the CAP dampens the outgoing wave in the asymptotic region. This means that the eigenfunction of the resonance state

can be solved for in a square-integrable basis, that is, one solves a complex matrix problem to find complex energy eigenvalues. The real part yields the resonance position, and the inverse of the imaginary part is associated with the lifetime of the state (c.f Eq. (1.1)). Accurate complex energy eigenvalues can be obtained by means of the Riss and Meyer (1.14), or by a Padé extrapolation method (1.19). The discretization procedure for the complex Hamiltonian Eq.(2.4) is analogous to the hermitean case discussed in Sect. 2.3.

2.5 Results and Discussion

In Fig. 2.2 we show the ionization rates for the lower and upper states as a function of internuclear separation R for the field strength of $F = 0.0533\,au$. The lower state shown in panel (a) displays monotonic behavior where the small rate at the equilibrium separation of $R = 2\,au$ rises gradually with R because the tunnelling barrier is easier to penetrate, as will be shown in subsequent figures. For the upper state the much larger ionization rate is non-monotonic and shows strong maxima at $R \approx 5.5\,au$ and at $R \approx 9\,au$ ($1\,au$ corresponds to $0.53\mathring{A} = 5.3 \times 10^{-11}\,m$).

In the latter graph we show how our results compare with the data of Chu *et al.*, [13] and Plummer and McCann [12]. Our data are in excellent agreement with those at small and intermediate R, and confirm the results of Ref.[13] at large R. Our extrapolation and higher-order Riss-Meyer results enable us to reach higher

accuracy than Chu *et al.*, and are presented below in Table 2.4.

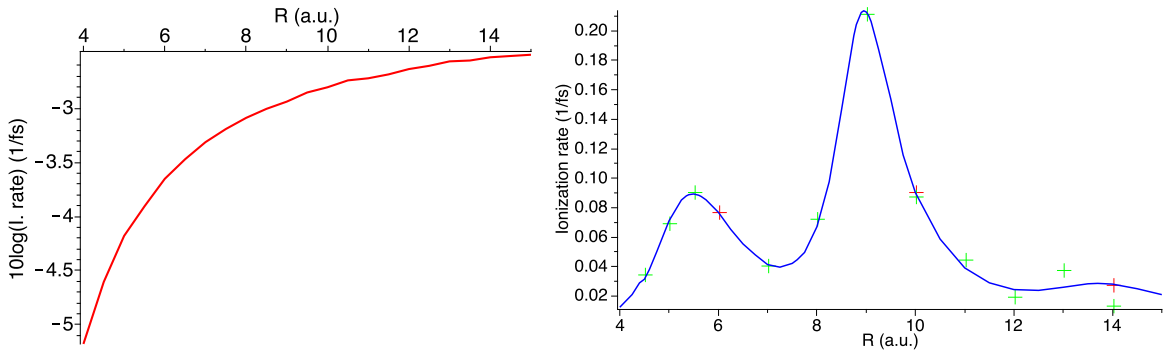

(a) (b)

Figure 2.2: Ionization rates (in fs^{-1}) for varying R for the lower (a), and the upper (b) states of H_2^+ for a field strength of $F = 0.0533\,au$. Curves: present results, red crosses: Chu *et al.*, [13], green crosses: Plummer and McCann [12].

To understand the intriguing behavior of the upper-state ionization rate we show plots that indicate the cross section through the potential along the internuclear axis, and also density plots for the resonance states for a few internuclear separations. In Fig 2.3a we observe on the basis of the eigenenergies how the lower state is trapped efficiently by the two-centre potential, while the upper state is above the potential barrier along the internuclear axis. The density plots in parts (b,c) of the figure display some preferential localization, as well as a still apparent nodal structure in the upper state. Nevertheless, both states can still be thought of as exploring the full two-centre potential. In the following we emphasize the behavior

found for the upper state, since the lower state follows a simple pattern: its tunneling barrier decreases gradually with separation R resulting in a monotonic increase in ionization rate. The upper state, on the other hand, exhibits de-localization and a shift in resonance position as compared to the barrier heights.

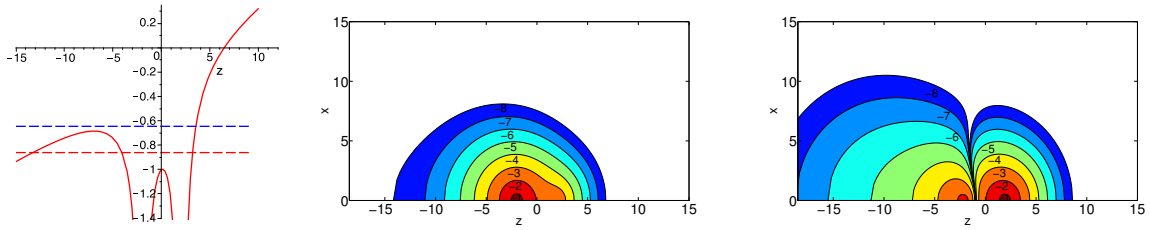

(a) (b) (c)

Figure 2.3: Electronic potential and real parts of quasienergies for the lower and upper states (a) and contour plots of $\log|\psi|^2$ for the lower (b) and upper (c) states for H_2^+ at $R = 4\,au$ and $F = 0.0533\,au$

In Fig. 2.4 we move to the situation where the upper state has a maximum in the ionization rate. The potential barrier between the two protons increases, while the outer potential barrier is lowered. The upper-state energy eigenvalue moves up with increasing R, which also results in a big increase of the ionization rate. The density plots reveal further localization for the central parts of the resonance wave function. The distant parts describe outgoing electron flux. Their relative weight is increased due to the broadening of the resonance state, and the upper state begins to lose its nodal structure.

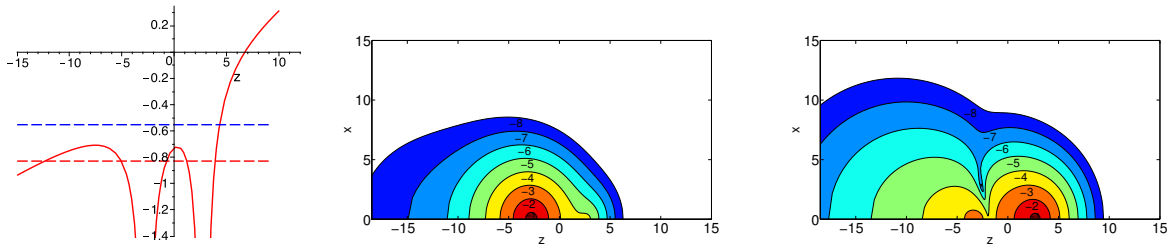

(a) (b) (c)

Figure 2.4: Same as in Fig. 2.3, but for $R = 5.5\,au$ and $F = 0.0533\,au$

Fig. 2.5 shows what happens at $R = 7\,au$, where the upper-state ionization rate has a pronounced local minimum, but is still much larger than at $R = 4\,au$. Panel (a) shows that the energetic conditions are less favourable for the upper state than in the $R = 5.5\,au$ case, because the inner barrier has risen faster than the energy eigenvalue. The separation of the bound parts of the wave functions of the lower and upper resonance states is now very distinct. The outflow of ionized electron density is more de-localized than for smaller separations.

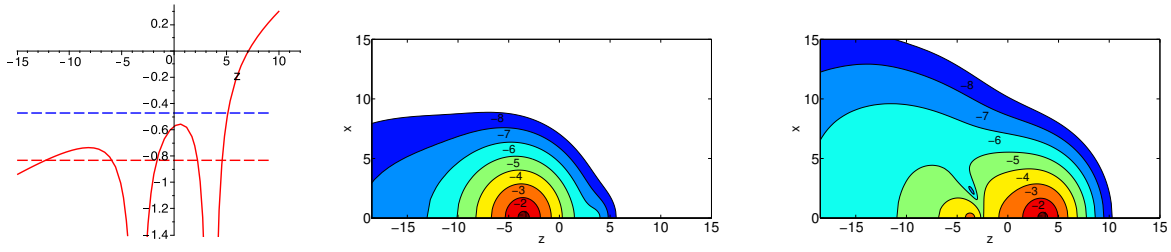

(a) (b) (c)

Figure 2.5: Same as in Fig. 2.3, but for $R = 7\,au$ and $F = 0.0533\,au$

In Fig. 2.6 we illustrate the situation for $R = 9\,au$, where the absolute maximum

in the upper-state ionization rate is achieved (at more than twice the level of the first maximum). The energy diagram shows that the inner barrier is catching up with the rising upper-state eigenvalue. From the density plot we can deduce that diffractive scattering is happening from a well-localized bound upper state (note that the lower state is very well confined in the left well), with sideways scattering, and forward scattering being the preferred pathways for electron emission.

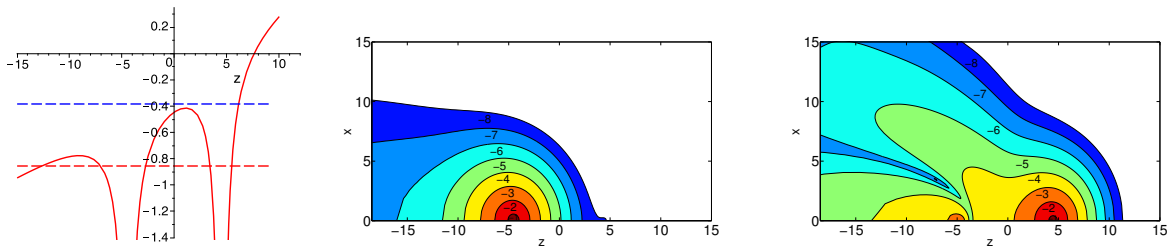

(a) (b) (c)

Figure 2.6: Same as in Fig. 2.3, but for $R = 9\,au$ and $F = 0.0533\,au$

Further increases in internuclear separation (Fig. 2.7 shows the situation for $R = 14\,au$) result in an increased inner barrier height for the upper state. Thus, its ionization rate remains relatively low. The density pattern indicates more diffractive electron emission with less flow in the direction of the internuclear axis.

In order to understand whether these findings are universal it is useful to consider other field strength values. We have carried out a detailed study of the case of $F = 0.04\,au$. The ionization rates for the lower and upper states are shown in Fig. 2.8 (a,b) respectively. The upper-state ionization rate curve again has two

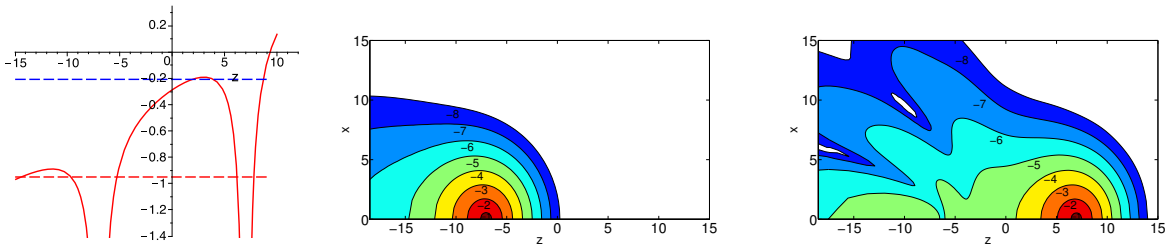

(a) (b) (c)

Figure 2.7: Same as in Fig. 2.3, but for $R = 14\,au$ and $F = 0.0533\,au$

maxima with an almost two-to-one ratio for the peak heights. Their positions are shifted to $R \approx 7.3\,au$ and $R \approx 11.2\,au$ respectively. As demonstrated in Fig. 2.9 for $R \approx 9.25\,au$ the minimum in the ionization rate for the upper state occurs when the eigenvalue is 'caught' by the rising potential barrier. Interestingly, for larger separations the barrier keeps rising, but the system ionizes efficiently by avoiding this region with more sideways electron emission. When going to larger separations ($R > 13\,au$), however, the trapping of the upper state becomes efficient. These findings mostly confirm the conclusions drawn by Plummer and McCann on the basis of complex scaling calculations using an algebraic basis function representation.

In Figure 2.10 we show surface plots of $\log|\psi|^2$ for the upper state of the H_2^+ ion which shows the largest peak at $R = 9\,au$ (Fig. 2.2b) and $R = 11\,au$ (Fig. 2.8b) respectively (Fig. 2.6c is the equivalent of Fig. 2.10a). Both panels (Fig. 2.10a, b) show that there is a large fold, which separates the electron flux along the internuclear axis from a second component emitted in the $30 - 50$ degree polar

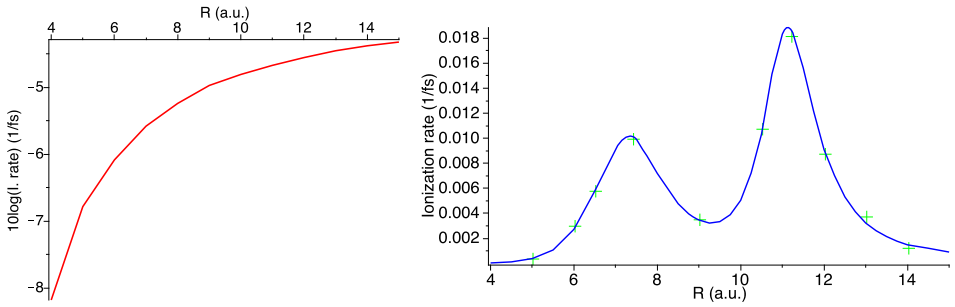

(a) (b)

Figure 2.8: Ionization rates (in fs^{-1}) for varying R for the lower (a), and the upper (b) states of H_2^+ for a field of strength $F = 0.04\,au$. Green crosses: results of Plummer and McCann [12].

angle range. Note that the results were obtained with a small value for M_ν (ν-axis) in the matrix calculation, but the global cardinal interpolation (1.68) was used for this axis to create the electron density plots.

We now turn to the problem of a more accurate determination of resonance parameters. In order to reach higher accuracy one needs to investigate two aspects of the problem. On the one hand, the solution of the discretized problem needs to be analyzed with respect to the parameters defining the discretization. On the other hand there is the issue that analytic continuation methods introduce the artifact of complex scaling or complex absorption. It is this second issue for which we show some detailed results.

In Fig. 2.11a we show four basic methods to extract information from the

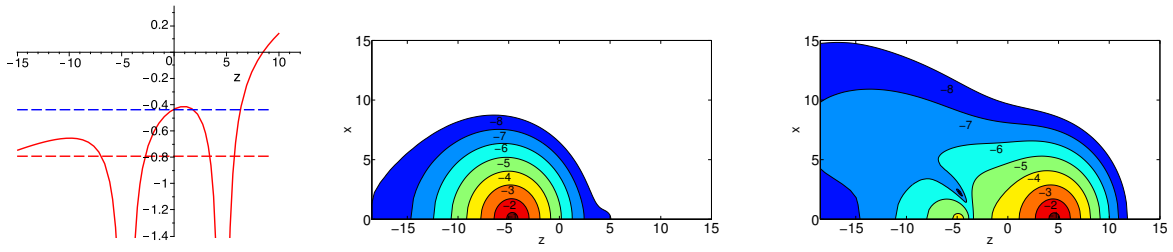

(a) (b) (c)

Figure 2.9: Same as in Fig. 2.3, but for $R = 9.25\,au$ and $F = 0.04\,au$

complex eigenvalue trajectories. Shown as red diamonds are the original finite-basis matrix eigenvalues E_{fb} near the stabilization value $\eta_{st} = \tilde{\eta}^{(0)}$ (red crosses). For η-values less than this stabilization value the trajectory displays erratic behavior, since the numerical method cannot handle the demand to compute an outgoing oscillatory solution. When using $N_p = 4$ accurate eigenvalues from a range of $\eta > \eta_{st}$ values a Padé approximation eq.(1.19) is solved, and this functional form is extrapolated to $\eta = 0$. This analytic η-trajectory is shown as a green curve.

Also shown in Fig. 2.11a are results from the first four orders $n = 0, \ldots, 3$ of the Riss-Meyer iterative correction scheme eqs. (1.14, 1.15). The trajectories $E^{(n)}(\eta)$ are shown parametrically (η is incremented in discrete equidistant steps), and it is evident that on the scale of the graph they have accumulation points eq. (1.15) very close to each other, and that the complex energy values at the accumulation points are very close for $n = 1..3$, but deviate from the stabilization method point ($n = 0$). The proximity of the $n = 3$ result to the Padé extrapolated value (which

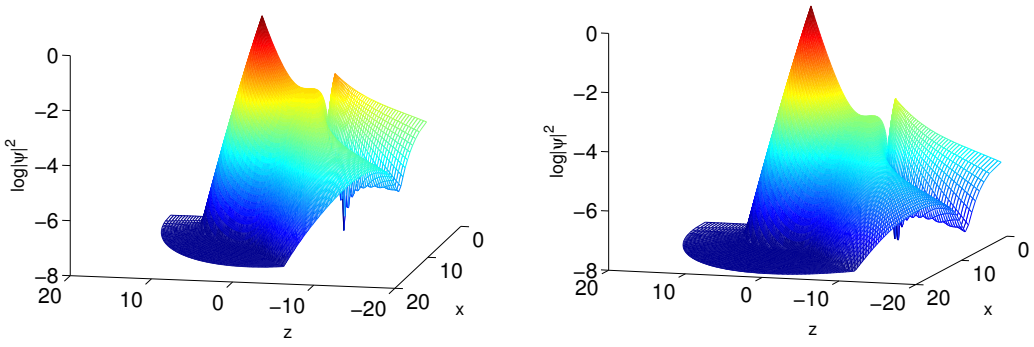

(a) (b)

Figure 2.10: Three-dimensional representation of $\log|\psi|^2$ for the upper state of the H_2^+ ion. (a) $R = 9\,au$ and $F = 0.0533\,au$; (b) $R = 11\,au$ and $F = 0.04\,au$.

is based on $E_{fb}(\eta)$) is also evident.

A magnification of the region close to the $n = 1..3$ accumulation points is shown in Fig. 2.11b. The acccumulation points given by eq.(1.15) are marked by crosses and are coinciding with many data points that fall on top of each other. With increasing order n the data are based on $E_{fb}(\eta)$ values calculated at larger η. For $n = 1$ (blue symbols) the results near the accumulation point come from the $\eta = 0.007..0.01$ range, for $n = 2$ (magenta symbols) from $\eta = 0.009..0.024$, and for $n = 3$ from $\eta = 0.013..0.042$. The Padé extrapolated results were based upon $\eta = 0.007..0.015$ with $\eta_{st} = 0.003$. The strength of the higher-n calculations comes, therefore, from the effective removal of the complex-absorber artifacts while using larger values of η. At these larger η-values the solution of the discretized

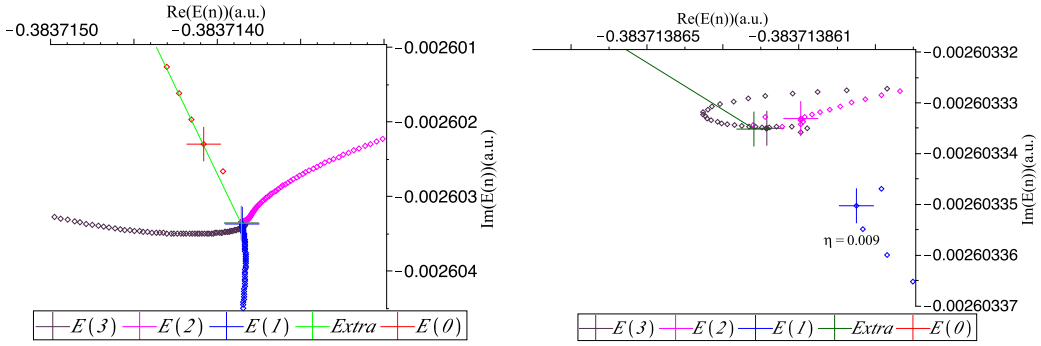

(a) (b)

Figure 2.11: The η-trajectories for $E^{(0)}$ (red diamonds), $E^{(1)}$ (blue diamonds), $E^{(2)}$ (magenta diamonds), and $E^{(3)}$ (black diamonds) for the upper state of the H_2^+ ion at $R = 9\,au$ and electric field strength $F = 0.0533\,au$. The red, blue, magenta and black crosses are for $E^{(n)}(\tilde{\eta}^{(n)})$ for $n = 0 \ldots 3$ respectively, while the Padé extrapolated value is shown as a green cross, and is the end point of the green line. The computational parameters are $N = 110, M = 14, \mu_c = 2.2$. Panel a gives a global view (three crosses overlap), while panel b shows a zoomed-in view.

complex Schrödinger problem is closer to the continuum limit, since it involves more localized wave functions which are more amenable to a finite representation.

Fig. 2.11b allows one to make an assessment of the accuracy level reached by the calculations. Ideally, one would like to demonstrate the convergence of the Riss-Meyer series, by showing higher-n results. In practice these results become affected by differentiation errors along the complex trajectory of $E_{fb}(\eta)$. A conservative

estimate of the error would be given by the difference between the $n = 2$ and $n = 3$ results. The Padé extrapolated value falls close to the $n = 3$ value. Further tests were performed by varying the value of μ_c. Within the range $1.5 < \mu_c < 3$ (in a.u.) the changes in the accumulation point value for $n = 3$ remained stable within the tolerance limit mentioned above.

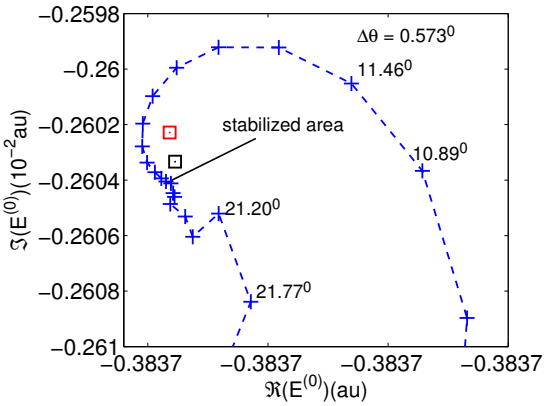

Figure 2.12: Complex scaling result for the θ-trajectory of $E^{(0)}$ for the upper state of the H_2^+ ion at $R = 9\,au$ and electric field strength $F = 0.0533\,au$. The red box indicates the $(n = 0)$ Riss-Meyer result, while the black box shows the converged result. The grid parameters are $N = 110$ and $M = 14$.

As an implementation of the CS method in the thesis, we show in Fig. 2.12 the θ-trajectory of the complex eigenvalue for the upper state of the H_2^+ ion at $R = 9\,au$. This θ-trajectory is equivalent to the η-trajectory (red diamond) in Fig. 2.11a. The complex eigenvalue is obtained from the diagonalization of the Stark Hamiltonian

(2.3) with the complex scaled coordinate of $\mu \rightarrow \mu e^{i\theta}$ (cf Eq.(1.9)). The red and black boxes indicate the ($n = 0$) Riss-Meyer (red cross in Fig. 2.11a) and the converged ($n = 3$) results. The widths obtained from the ($n = 0$) Riss-Meyer and stabilization methods are $\Gamma^{(0)} = 5.2046\,10^{-3}\,au$ and $\Gamma^{(st)} = 5.2082\,10^{-3}\,au$ with $\theta_{st} = 17.76^0$, respectively. These values are seen to be accurate up to 3 significant digits, when compared to the precise values shown in Table 2.4. It is evident that the ($n = 0$) Riss-Meyer CAP result is not very close to the stabilized CS area, and that the converged result is somewhat closer to that area (cf Fig. 2.12).

2.6 Summary

In this chapter we extended previous complex scaling calculations for the Stark resonance problem of the hydrogen molecular ion, which were performed both in algebraic [11, 12] and pseudospectral representations [13] to a higher degree of accuracy. This was achieved by implementing several orders of the Riss-Meyer correction scheme to the complex eigenvalues obtained from a pseudospectral calculation with complex absorbing potential and also by using the Padé extrapolation method.

The surprising behavior of the ionization rate of the upper state (localized in the higher well) as a function of internuclear distance was illustrated by density plots of the localized decaying state (whose long-range tails are suppressed by the complex absorber). The computation in prolate spheroidal coordinates was found

to be highly efficient.

A natural extension of this work is the AC Stark problem which can be accomplished using a Floquet approach. If one assumes that the strong modulation of the upper-state ionization rate with intermediate separation described in this chapter persists in the case of infrared laser fields, then it follows that the detailed analysis of experiments [60] will be affected by this phenomenon. In the following chapter we will investigate the AC Stark problem.

Table 2.4: The calculated DC widths Γ_{low} and Γ_{up} of the lower and upper states of H_2^+ for field strength $F = 0.0533\,au$ using the stabilization method (SM), Padé extrapolations (PE), and the order ($n = 3$) Riss-Meyer scheme. Also shown are the earlier calculations of Zuo and Bandrauk [10], Mulyukov *et al.*, [11], and Xi Chu and Shih-I Chu [13]: The stablilization results (SM) are equivalent to the ($n = 0$) RM results, and the Padé extrapolation is based on complex eigenenergies calculated directly from the non-hermitian matrix problem for η-values not far from the SM result $\eta_{\rm SM}$ ($\eta > \eta_{\rm SM}$).

	R=6 au		R=9 au	
	$\Gamma_{low}(au)$	$\Gamma_{up}(a.u.)$	$\Gamma_{low}(au)$	$\Gamma_{up}(au)$
Ref.[10]	2.2(−6)	9.8(−4)		
Ref.[11]	5.69(−6)	1.87(−3)		
Ref.[13]	5.692(−6)	1.873(−3)		
SM	5.645 17(-6)	1.870 80(-3)	2.958 14(-5)	5.204 57(-3)
PE	5.692 38(-6)	1.873 34(-3)	2.970 75(−5)	5.206 67(−3)
RM (n = 3)	5.692 38(−6)	1.873 34(−3)	2.970 75(−5)	5.206 67(−3)
	R=10 au		R=14 au	
	$\Gamma_{low}(au)$	$\Gamma_{up}(au)$	$\Gamma_{low}(au)$	$\Gamma_{up}(au)$
Ref.[10]	1.3(−5)	1.5(−3)	2.5(-5)	2.8(-4)
Ref.[11]	3.92(−5)	2.20(−3)	7.30(-5)	6.78(-4)
Ref.[13]	3.922(−5)	2.197(−3)	7.305(−5)[1]	6.778(-4)
SM	3.896 99(-5)	2.197 47(-3)	7.304 87(-5)	6.778 81(-4)
PE	3.922 55(-5)	2.196 79(-3)	7.305 23(-5)	6.778 27(-4)
RM (n = 3)	3.922 55(−5)	2.196 79(−3)	7.305 23(-5)	6.778 27(-4)

3 AC Stark resonance parameters for the hydrogen molecular ion in an intense linearly polarized laser field

In this chapter, we discuss the AC Stark resonance parameters for the hydrogen molecular ion in an intense linearly polarized laser field. This theoretical investigation can be seen as an extension of work discussed in Chapter 2. We begin with an introduction to the problem in Sect. 3.1 and continue the basic formulation of the AC Stark resonance Hamiltonian in Sect. 3.2. The computational results and their discussion are presented in Sect. 3.3. which is followed by a summary.

Originally published as Ts. Tsogbayar and M. Horbatsch, J. Phys. B: At. Mol. Opt. Phys. **46** 245005 (2013).

3.1 Introduction

The study of ionization of atoms and molecules by continuous-wave (CW) strong-field lasers in the optical and infrared regimes has evolved to a good level of understanding. Dissociative ionization of small molecules was reviewed in [1]. Experimentally, the focus has shifted toward short pulses, since pulse compression allows for stronger fields, but studies of the hydrogen molecular ion in intense laser fields were also carried out in the CW regime [2], particularly for infrared light [61]. Theoretically, the continuous-wave case can be treated by standard Floquet theory, while short pulses are dealt with by solving the time-dependent Schrödinger equation directly [62]. In addition, multi-mode Floquet analysis allows to take a pulse envelope into account [63]. While much focus has shifted towards understanding detailed phenomena, such as electron spectra and high harmonic generation from many-electron molecules [64], there is still some need to explore ionization rates as a function of internuclear separation R for the simplest molecule, namely the hydrogen molecular ion H_2^+.

The interest in the $R-$dependent ionization rates for the lowest molecular eigenstates arises for several reasons: in laser-pulse experiments the neutral molecule is often ionized by the rising pulse and produces a molecular ion in a dissociating state, i.e., a high vibrational mode of the molecule is excited [65, 66]. The strong

field may also mix the lowest two electronic eigenstates. As the molecule expands the ionization rates for both states increase substantially, and the laser may ionize the molecule efficiently at so-called critical separations R_c [61]. Vibrational population trapping is also predicted [67]. It is possible to determine the actual distance R when ionization occurred from a measurement of the kinetic energies of the molecular fragments [2].

Experiments were thus able to confirm at least parts of the pattern of the ionization rate vs R obtained from theoretical calculations. However, the structures in the ionization rate predicted for larger internuclear separations R could not be found in some experiments [9]. Other experiments with carefully prepared H_2^+ ions with short (100 fs) laser pulses and a wavelength of 791 nm were able to find evidence of three larger-R maxima in the ionization rate [68, 69].

Structures in the $R-$dependent ionization rate were found theoretically in the DC limit [11, 12, 13, 58] for the upper state as demonstrated in Chapter 2. The physical mechanism for strong-field ionization in this limit is tunneling for the lower state, and small-barrier tunneling or over-the-barrier escape for the upper state depending on the field strength and separation R. The calculations are deemed mature, with different methods confirming earlier results, and resulting in a high degree of precision in the resonance positions and widths for the single-electron molecule. Interestingly, the peaking structures in the ionization rate for the upper

state are quite similar to those of AC Stark calculations. It is therefore interesting to search for a connection, and particularly to explore the small-ω limit of the AC case.

In atomic photoionization one can distinguish between the tunneling and multiphoton ionization regimes with the help of the Keldysh parameter, defined as $\gamma = \sqrt{|E_b|/2U_p}$ where E_b is the electron binding energy and $U_p = (F/2\omega)^2$ is the pondermotive energy with F the laser electric field strength and ω the angular frequency in atomic units. A value of $\gamma \ll 1$ corresponds to tunneling ionization, $\gamma \sim 1$ indicates the intermediate regime, and for $\gamma \gg 1$ we expect multiphoton ionization. In Table 3.1 we show the values of the Keldysh parameter for some chosen values of wavelength λ and a field intensity of $I = 10^{14}\, W\, cm^{-2}$, for the ground and first excited states of the H_2^+ ion.

It is known, however that in the molecular case matters are more complicated, especially at intermediate internuclear separations R [70]. The complicated behavior was associated with non-adiabatic electron localization near the nuclei. Some peculiar electron localization was evident in results in Sect. 3.3.

The Floquet-analysis of the strong-field AC Stark problem was pioneered for atomic hydrogen by Shakeshaft and co-workers [71]. For the hydrogen molecular ion the $R-$dependent peak structures were analyzed by Madsen and Plummer [72] with ideas based on Floquet channel couplings to identify which mechanism was

Table 3.1: The values of the Keldysh parameter for the $1s\sigma_g$ and $2p\sigma_u$ states of the H_2^+ ion at various separations R (in au), and laser intensity $I = 10^{14}\, W\, cm^{-2}$.

	$\lambda\,(nm)$	ω	$R=2$	$R=4$	$R=6$	$R=8$	$R=10$	$R=12$
$1s\sigma_g$	1064	0.0428	1.18	1.01	0.93	0.89	0.88	0.87
	2280	0.02	0.56	0.47	0.44	0.42	0.41	0.40
	4560	0.01	0.28	0.24	0.22	0.21	0.21	0.20
$2p\sigma_u$	1064	0.0428	0.93	0.95	0.92	0.90	0.88	0.87
	2280	0.02	0.43	0.44	0.43	0.42	0.41	0.40
	4560	0.01	0.22	0.22	0.21	0.21	0.21	0.20

responsible for them: as an alternative to tunneling they offered explanations in terms of resonance-enhanced multi-photon ionization (REMPI).

In a naive, intuitive picture one might think that in the presence of a tunneling barrier the small-ω limit implies that ionization is effective only during the peak of the field: during a cycle this will occur twice (once to each side), and re-scattering of electrons ionized during earlier cycles will also take place. The Floquet picture, on the other hand, suggests that photo-ionization in a small-ω CW laser field is a complicated process, requiring the coupling of very many channels to make an accurate prediction. It also suggests that the lower and upper states become highly mixed. It appears then that the Keldysh parameter values which decrease with ω are perhaps misleading in the molecular case. This is obviously the case for the upper state which is not affected by an outer potential barrier at intermediate and

large R. As will be shown below, the lower state is mixing with the upper state in this R-regime, and, thus, the Keldysh argument has to be used carefully in the molecular intermediate-R case even for the lower state.

The purpose of our work is to illustrate the Floquet results systematically in the limit of small laser frequency. Using a methodology similar to previous work at $\lambda = 1064\,nm$, we confirm a number of prior results and also find some discrepancies. New features are found as the IR wavelength is pushed further into the μm regime.

3.2 AC Stark-resonance Hamiltonian and CAP method

Since we gave basic descriptions of how the Floquet method is applied for a time-periodic physical system in Section 1.2, and for the computational procedures to solve the Schrödinger equation for the H_2^+ ion in subection 1.3.7, we will not discuss them in this subsection.

Following Eqs. (1.30-1.31) we have the time-independent coupled-channel matrix equations for the AC Stark-resonance problem for the H_2^+ ion:

$$[H_0(\mu,\nu) - i\eta^{(0)}W(\mu)]\phi_n(\mu,\nu) + \frac{1}{2}Fz[\phi_{n-1} + \phi_{n+1}] = (E_F - n\omega)\phi_n(\mu,\nu),$$
$$(n = 0, \pm 1, \pm 2 \ldots) \quad (3.1)$$

in length gauge, and

$$[H_0(\mu,\nu) - i\eta^{(0)}W(\mu)]\phi_n(\mu,\nu) + \frac{1}{2}\frac{F}{\omega}\frac{\partial}{\partial z}\Big[\phi_{n-1} - \phi_{n+1}\Big] = (E_F - n\omega)\phi_n(\mu,\nu),$$

$$(n = 0, \pm 1, \pm 2 \ldots) \quad (3.2)$$

in velocity gauge. Here $H_0(\mu,\nu)$ is the field-free Hamiltonian (c.f Eq. (1.67)) and $\partial/\partial z$ is given as:

$$\frac{\partial}{\partial z} = \frac{2}{R(\mu^2 - \nu^2)}\Big[\nu(\mu^2 - 1)\frac{\partial}{\partial \mu} + \mu(1 - \nu^2)\frac{\partial}{\partial \nu}\Big], \quad (3.3)$$

and the form of the CAP $W(\mu)$ can be chosen as given in (2.4).

In equation (3.2) we removed the overall phase proportional to F^2, as it does not affect the results. The discretization of equations (3.1) and (3.2) is carried out similarly as we discussed in Section 1.3.7, that is, we do not symmetrize the Hamiltonian, which yields improved computational efficiency. We arrived at this conclusion by comparing the convergence properties of bound-state pseudospectral representations given in Ref.[73]. Photoionization of H_2^+ by short UV laser pulses has been treated recently by analogous grid methods for the time-dependent Schrödinger equation [74, 75, 76].

The real part of the complex energy eigenvalue from equation (3.1) or (3.2) gives the Stark shift due to the external laser field, while the imaginary part enables to obtain the ionization rate for any particular state of the ion. Therefore, one can view the AC Stark Floquet treatment as an extension of the DC case to a coupled-

channel problem. Interestingly, however, it will turn out that in the $\omega \to 0$ limit of the AC case the number of Floquet channels to be taken into account increases as $1/\omega$. This implies that the connection between the $\omega \to 0$ AC limit and the DC case is formally non-trivial.

3.3 Results and Discussion

In Fig. 3.1 we show results for the previously studied case of $\lambda = 1024\,nm$ where the Keldysh parameter is of order unity (the intensity of the laser field equals $10^{14}\,W/cm^2$). The ionization rates as a function of separation R (obtained as $-2\Im(E_F)$ (cf. Sect. 1.2.1)) are shown in panel (a) for the lower and upper states starting from the equilibrium value ($R = 2\,au$). The lower state has a very small ionization rate for $R < 4\,au$ due to the large outer tunnelling barrier. The upper-state ionization rate has a complicated pattern with distinct peaks at $R = 5.5\,au$ and $R = 7.75\,au$. The lower-state ionization rate rises to match the upper-state rate between the peaks, and then surpasses the upper-state rate (peak at $R = 9.5\,au$).

Our results are in reasonable agreement with those of Chu and Chu [13] with some notable differences in the region beyond the first peaks. We carried out a substantial convergence analysis to confirm our results in both the length and velocity gauges. The convergence properties of the Floquet calculations in velocity vs length gauge can be characterized as follows. As is shown in Table 3.2 for larger

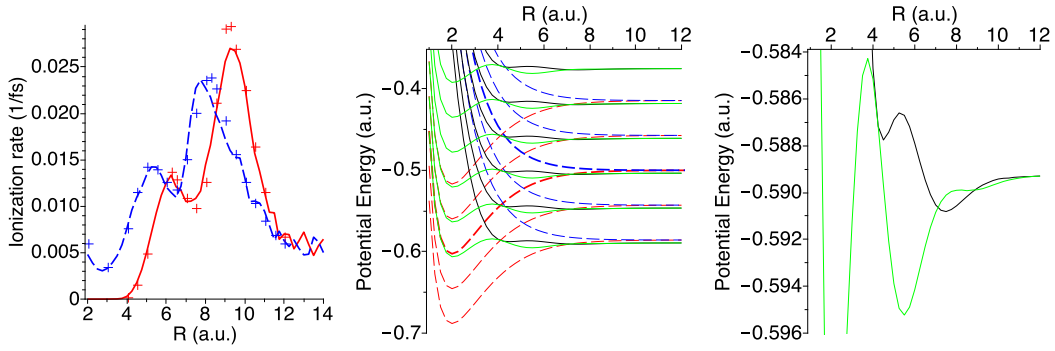

(a) (b) (c)

Figure 3.1: (a) The ionization rates (in fs^{-1}) as functions of R for the lower and upper states of H_2^+. Curves: present results, solid red for the lower state, and dashed blue for the upper state; crosses: Chu et al [13]: (b) for the lower and upper states of the ion, the field-dressed diabatic potential red (lower) and blue (upper) curves are dashed, respectively, and the corresponding adiabatic potential curves are presented by solid green (lower) and black (upper) curves: (c) the magnified detail of (b), showing clearly true and avoided crossings for the adiabatic potential curves. The field parameters are $F = 0.0533\,au$ and $\omega = 0.0428\,au$.

ω than of interest in this work, such as $\omega = 0.2\ au$ at the equilibrium proton separation of $R = 2\ au$ we found convergence in resonance position and width for the upper state to be better than seven digits for 21 channels in velocity gauge, and 25 channels in length gauge. At a wavelength of $\lambda = 1024nm$, or $\omega = 0.0428\ au$ 57 channels were required in length gauge to achieve this accuracy, while a 65-channel calculation in velocity gauge only resulted in absolute 5-digit accuracy. For

$\omega = 0.02\ au$ the length gauge calculation was 7-digits accurate at 49 channels, while the velocity gauge yielded poor results even at 65 coupled channels. Therefore, the length gauge was deemed most appropriate for the low-ω work which we pursue here to connect with the DC limit.

Table 3.2: Resonance parameters for the upper state of the H_2^+ ion at $R = 2\,au$ as a function of the number of Floquet channels N_F for field strength $F = 0.0533\,au$.

$\omega\,(au)$	N_F	$E^{(0)}\,(au)$, $(len.g)$	$E^{(0)}\,(au)$, $(vel.g)$
0.2	5	-0.669 911 377 - 0.001 943 7960i	-0.679 278 4768 - 0.000 072 5227i
	9	-0.678 498 1385 - 0.004 863 1700i	-0.673 211 56140 - 0.005 028 3890i
	13	-0.674 426 0573 - 0.004 846 4693i	-0.674 297 3716 - 0.005 435 1860i
	17	-0.674 279 7154 - 0.005 426 1126i	-0.674 292 5023 - 0.005 439 3768i
	21	-0.674 292 4336 - 0.005 439 3471i	-0.674 292 5623 - 0.005 439 3323i
	25	-0.674 292 5620 - 0.005 439 3325i	-0.674 292 5621 - 0.005 439 3322i
0.0428	17	-0.671 701 3524 - 0.000 092 9366i	-0.671 440 5537 - 0.000 000 3390i
	25	-0.671 731 0589 - 0.000 061 6783i	-0.671 709 5922 - 0.000 004 1644i
	33	-0.671 720 1980 - 0.000 058 1504i	-0.671 686 5629 - 0.000 071 8933i
	41	-0.671 721 9121 - 0.000 058 3764i	-0.671 721 6609 - 0.000 058 8151i
	49	-0.671 721 8571 - 0.000 058 4393i	-0.671 719 7192 - 0.000 059 0233i
	57	-0.671 721 8556 - 0.000 058 4388i	-0.671 719 9086 - 0.000 058 9689i
	65	-0.671 721 8556 - 0.000 058 4388i	-0.671 719 9214 - 0.000 058 9881i
0.02	17	-0.671 603 3844 - 0.000 019 7701i	-0.666 165 0263 - 0.000 000 0018i
	33	-0.671 603 9417 - 0.000 019 1176i	-0.666 854 7369 - 0.000 000 0897i
	49	-0.671 603 9751 - 0.000 019 1690i	-0.670 274 1425 - 0.000 000 8449i
	65	-0.671 603 9544 - 0.000 019 1759i	-0.670 316 3958 - 0.000 011 3380i

In Fig. 3.1b we show the Floquet potential energy curves. One can understand

the mixing of the lower and upper states for $R > 4\,au$ on the basis of this diagram. The field dressed diabatic potential curves for the lower and upper states are shown by dashed red (lower) and dashed blue (upper) curves, which are obtained from Eqs (3.1) or (3.2) in the absence of an external field, i.e, for $F = 0$. The non-diagonal coupling term caused by the external field vanishes in this limit, and the eigenvalues of the *hermitean* Hamiltonian yield the diabatic curves. These diabatic curve pairs are shifted from each other by $\pm n\omega$, where n is the number of photons absorbed or emitted [72]. The bold dashed red and blue curves represent the zero-photon lower $(1s\sigma_g - 0\omega)$ and upper $(2p\sigma_u - 0\omega)$ states. While the lowest diabatic curve for the lower state shown in (b) corresponds to the $1s\sigma_g - 2\omega$ state, the highest diabatic curve for the upper state represents the $2p\sigma_u + 2\omega$ state.

The lower/upper state curves for different values of n undergo true crossings. The corresponding adiabatic potential curves for the lower and upper states are represented by solid green (lower) and solid black (upper) curves, which are obtained in presence of the external field, that is, from the full non-hermitean resonance Floquet Hamiltonian calculation (3.1) or (3.2). These adiabatic curves undergo avoided crossings where true crossings occur in the diabatic levels. The complex energies are not allowed to cross (the Hamiltonian depends adiabatically on R). The crossings have to be of avoided type since degeneracies in a Hamiltonian spectrum correspond to some symmetry. No symmetry is, however, expected when varying

R in the Hamiltonian.

In panel c) of Fig. 3.1 the potential energy curves for the $n = 0$ Floquet channel are shown on a fine scale. Following the methodology of Madsen and Plummer [72] (based on [71]) we tracked carefully the real and imaginary parts of the Floquet eigenvalues as a function of R. The crossing is avoided either in the real or in the imaginary part. A true crossing in the real part of of the complex energy is associated with an avoidance structure in the imaginary part, i.e., the ionization rate acquires complicated behaviour with maxima and minima as a function of R.

Then it should be noted that according to the methodology of Madsen and Plummer [72] the first peak shown in Fig 3.1 (a) is indeed a REMPI peak, because it is fully characterized by either an avoided crossing in $\Re(E_{res})$ and a true crossing in $\Im(E_{res})$ of the Floquet eigenenergy as the internuclear separation R varies, or the reverse situation.

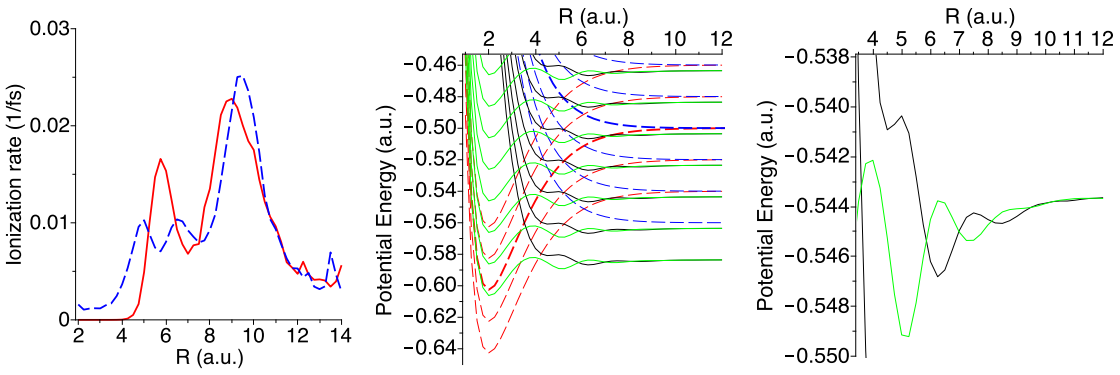

(a) (b) (c)

Figure 3.2: The same as in Figure 3.1, but $F = 0.0533\,au$ and $\omega = 0.02\,au$.

In Figs. 3.2 and 3.3 we proceed with the same strategy to understand the behaviour as the laser wavelength is moved further into the infrared regime. The following picture emerges: starting with $R > 4\,au$ the ionization rates for the two states intertwine; in the first peak region ($R \approx 5.5\,au$) this intertwining phenomenon is oscillatory with the number of oscillations increasing with decreasing ω. In the second peak region ($R \approx 9.5\,au$) the ionization rates for the upper and lower states track each other with apparently a better match as ω is lowered.

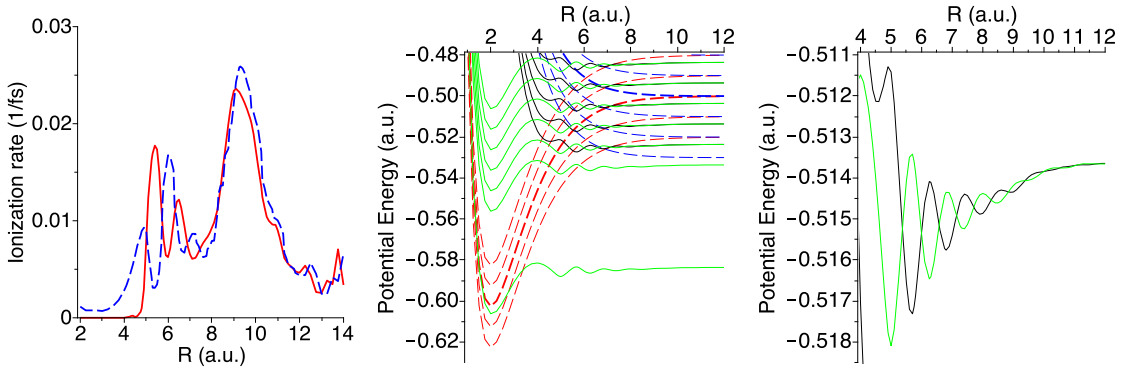

(a) (b) (c)

Figure 3.3: The same as in Figure 3.1, but $F = 0.0533\,au$ and $\omega = 0.01\,au$.

Panels b) and c) of Figs. 3.2 and 3.3 show the systematic reasons for the observed behaviour. On the energy scale set by the two molecular eigenstates as a function of R the number of participating Floquet channels increases as ω is reduced. While the panels (b, c) of the figures show only a limited number of Floquet channels, converged resonance parameter values were calculated on the

basis of at least $N_F = 64$ ($\omega = 0.0428\,au$), $N_F = 80$ ($\omega = 0.02\,au$) and $N_F = 100$ ($\omega = 0.01\,au$) channel calculations.

We have carried out calculations for smaller ω (further reduced by a factor of 2) with the finding that the number of oscillations in the region of the first peak keeps increasing (Figure 3.4). These calculations are more time-consuming, as the number of Floquet channels to be coupled increases correspondingly.

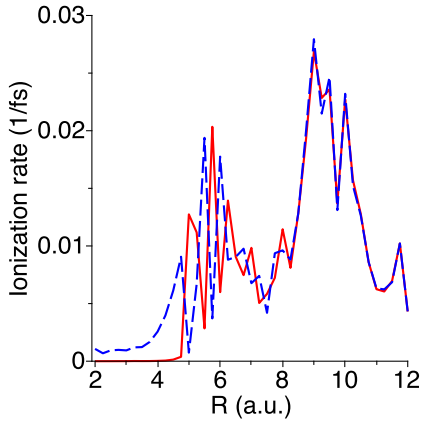

Figure 3.4: The same as in Figure 3.1a, but $F = 0.0533\,au$ and $\omega = 0.005\,au$.

From the comparison of the ionization rates shown in Figs 3.1-3 (a) and 3.4 we can make an interesting observation: the scale of the ionization rate appears to be quite independent of ω. We note that the widths of the Floquet resonances are still quite reasonable (below $10^{-3}\,au$), which means that the assumption of exponential decay which is built into the theory is reasonable.

A physical reason for the independence of the ionization rate on the laser fre-

quency ω can be given on the basis of the ionization mechanism. In the strong-field regime ionization can be understood via tunneling or as over-barrier escape mechanisms occurring for certain periods of time during the laser cycle (when the field is close to its peak value). Strong ω dependence can be expected in a multi-photon regime. From the present work it becomes clear that electron localization in one of the two wells is happening near the critical radii, and this is determining the upper- and lower-state ionization rates. The ω parameter plays an important role in the technical aspects of the calculation only, since it controls the number of Floquet channels which participate.

In Chapter 2 it was shown for the DC Stark problem how the peak structures in the ionization rates were associated with changes in the pattern of the localized probability density of the decaying Siegert states. For the AC case an analogous presentation is more complicated due to the time-dependence (during one period of the laser field $T = 2\pi/\omega$). We provide such a presentation in Figs 3.5 and 3.6 for the case of $\omega = 0.01\,au$ in order to illustrate the oscillatory pattern in the ionization rate. We chose two separations: in Fig. 3.5 for $R = 5.5\,au$ the lower state has a local maximum, while the upper state has a minimum in the ionization rate; in Fig. 3.6 for $R = 6\,au$ the situation is reversed.

The plots represent the time when the field is at its peak, i.e., they represent a snapshot of the density which has moved to the left with the laser field. For the

range of small ω values used in this work these (left-right) oscillations track the field oscillation reasonably well.

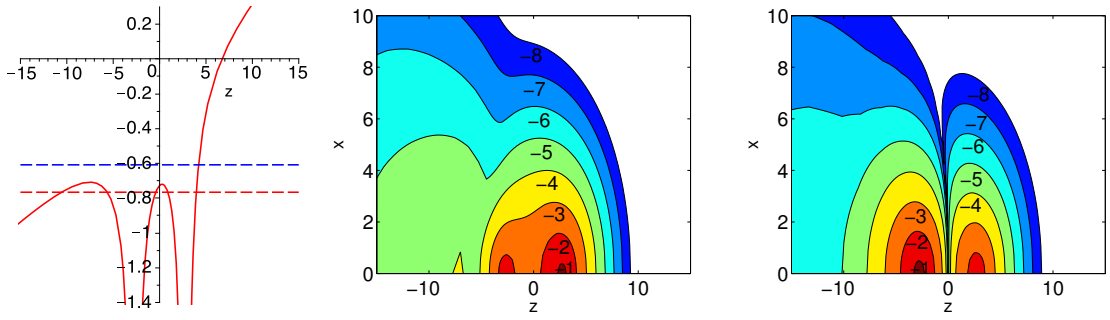

(a) (b) (c)

Figure 3.5: (a) Electronic potential and real parts of electronic quasienergies for the lower and upper states (reference channel $n = 0$) and (b,c) contour plots of $\log|\Phi(\mathbf{r}, t = 0)|^2$ for the lower, and upper states for H_2^+ at $R = 5.5\,au$, and $F = 0.0533\,au$ and $\omega = 0.01\,au$. The x- and z-axis are labeled in au.

Panels a) of Figs 3.5 and 3.6 show cuts through the potential along the molecular axis (at $t = 0, T$), as well as the resonance positions for both states (which are averaged over one cycle). They show the lower state as trapped (internal and external barrier), and the upper state as untrapped for both separations.

A comparison of the densities for the lower state shows that at $R = 5.5\,au$ (Fig. 3.5b) the state is more concentrated in the right well, and therefore ionizes rather easily (over-the-barrier mechanism). At $R = 6\,au$ (Fig. 3.6b), on the other hand, the lower state displays more localization in the left well, resulting in a reduced

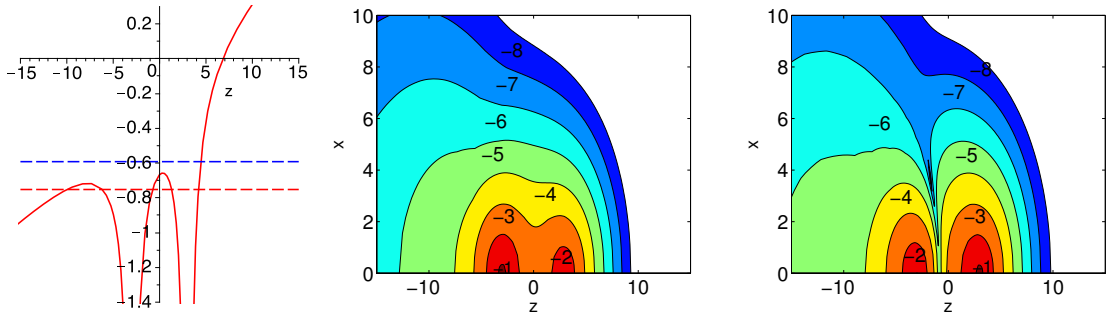

(a) (b) (c)

Figure 3.6: The same as in figure 3.5, but at $R = 6\,au$, and $F = 0.0533\,au$ and $\omega = 0.01\,au$.

ionization rate. This shows that the simple diagram (Fig. 3.6a) is insufficient to explain the ionization rate behaviour: the fact that the lower state localizes in the right-hand well for $R = 5.5\,au$ gives it apparently the 'over-the-inner-barrier' higher ionization property rather than tunneling behaviour.

This localization (or state-mixing) issue is the main reason why one has to be careful in applying the Keldysh parameter argument, which usually works well for atoms and equilibrium-R molecules. In the language of Floquet theory this state mixing is referred to as resonance enhanced multiphoton ionization [72].

The upper-state densities (Fig. 3.5c and 3.6c) show a reversed behaviour. The lower- and upper-state densities are distinct from each other: one can clearly see the remnants of a nodal structure of the field-free upper state (low-density region to the left of $z = 0$), while the lower state resembles the symmetry character of the

field-free state in the internuclear region.

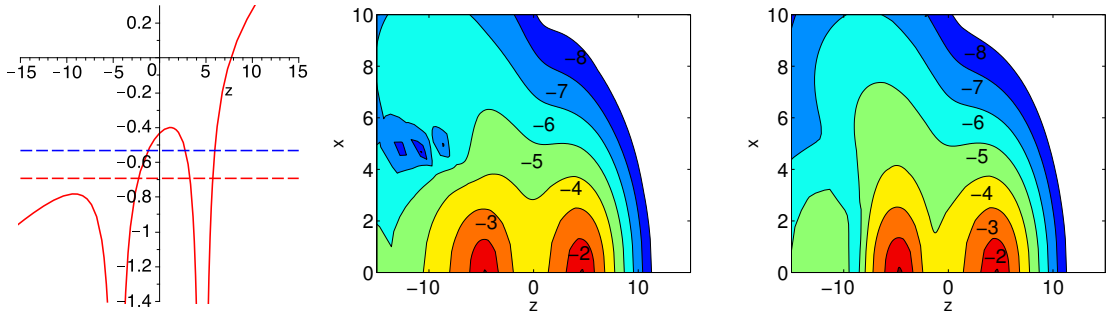

(a) (b) (c)

Figure 3.7: The same as in figure 3.5, but at $R = 9.25\,au$, and $F = 0.0533\,au$ and $\omega = 0.01\,au$.

Therefore, one can argue on the basis of the density plots that Floquet channel couplings occur in such a way that in the region of the first peak in the ionization rate the states maintain some of their identity even though their complex energies become intertwined. As one varies the separation R the lower-state density has maxima at either nucleus that vary dramatically in height. This causes the ionization rate to be strongly modulated as R is varied. The upper state has a complementary oscillation pattern. These density plots give support to the ideas of adiabatic electronic localization raised in Ref.[70].

For large R, when there is an inner tunneling barrier, the density localized near the nuclei oscillates with period $T = 2\pi/\omega$. For small ω it can, in fact, oscillate out of phase with the external field. While the individual stationary Floquet channel

functions $\phi_n(\mathbf{r})$ are either symmetric or anti-symmetric, their superposition with complex amplitudes $e^{in\omega t}$ can display tunneling oscillations with period T.

Finally, we show in Fig. 3.7 also a density plot for the larger-R peak region, namely near the maximum in the ionization rate ($R = 9.25\,au$). The energy levels superimposed on a snapshot of the potential along the molecular axis show that both states are energetically above the outer barrier in this case, but that there is an inner barrier to overcome. Both states have similar density patterns, i.e., the upper state has lost its nodal structure completely (as was observed for the DC case in Chapter 2). Thus, we can assume that complete state-mixing occurs in the region of the larger-R peak. Eventually, with increasing R the inner barrier rises, and ionization becomes less effective.

From Figs. 3.5-7 (a) it can be seen that the first peak in the ionization rate can be naively explained by the over-the-barrier mechanism: as R varies, the lower state shifts up and experiences less of an outer barrier. The second peak in the ionization rate is associated with the charge-resonant enhanced ionization (CREI) according to Bandrauk *et al* [10]. According to this theory the charge-resonant (CR) states are responsible for this anomalous enhancement and for these states the time-independent dipole moment diverges linearly as $R/2$ for large R where the charge distributions of the two states are almost the same (charge resonance) and their energies become nearly degenerate. While looking at the plots of the charge

density shown in panels (b,c) of Figure 3.7, they have almost the same features, which indeed supports the CREI mechanism.

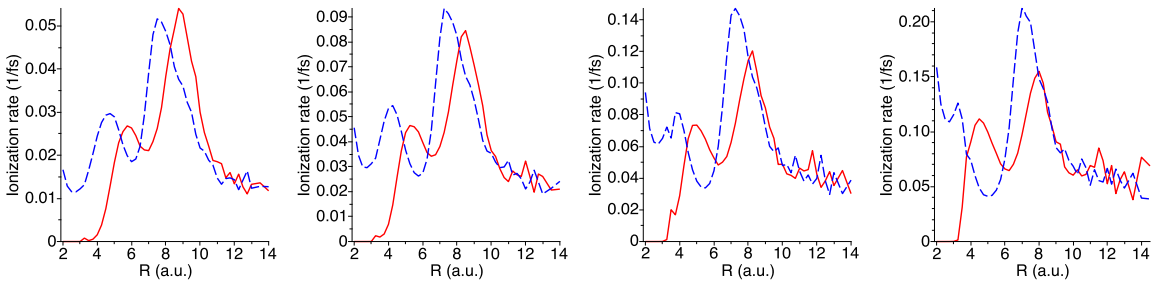

(a) (b) (c) (d)

Figure 3.8: The ionization rates (in fs^{-1}) as functions of R for the lower and upper states of H_2^+. Curves: present results, solid red for the lower state, and dashed blue for the upper state. (a) $F = 0.05968\,au$: (b) $F = 0.06538\,au$: (c) $F = 0.07062\,au$: (d) $F = 0.07549\,au$, and $\omega = 0.0428\,au$.

In Fig. 3.8 we present some additional results to show how the ionization rates change with laser intensity. It can be seen that for moderately stronger fields some changes in the ionization patterns can be found for small and intermediate R values. While the lower state for $R << 4\,au$ is still governed by tunnelling ionization, the regime where it mixes with the upper state begins at $R \approx 4\,au$ for the doubled intensity. The ionization rate for the upper state increases dramatically even at the equilibrium separation. For the outer critical radii we notice that they are also somewhat reduced with the lower state experiencing a less dramatic increase

in ionization rate. When we average the outer peaks for the two states we find approximately a seven-fold increase in ionization rate with doubled intensity. The intermediate cases (panels b, c) indicate that the changes occur gradually.

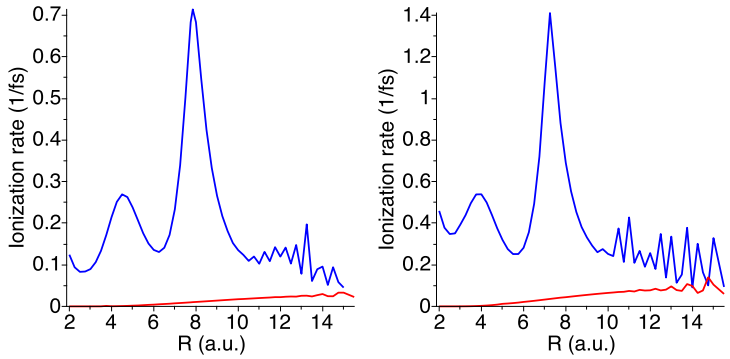

(a) (b)

Figure 3.9: The DC-limit ionization rates (in fs^{-1}) as functions of internuclear separation R for the lower (red) and upper (blue) states of H_2^+. The DC field strengths are $F = 0.06538\,au$ (a) and $F = 0.07549\,au$ (b).

In order to test our conclusions about the relation of the results to those for the DC limit for the upper state we show the latter results for two laser intensities in Fig. 3.9. These results (which are much easier to obtain technically, as there is no channel convergence to worry about and the analysis of the complex eigenvalue spectrum is straightforward) also show similar features as the field intensity increases: at the outer critical radius ($R_c \leq 8\,au$) we find an approximately seven-fold increase in ionization rate (for the upper state) when doubling the field

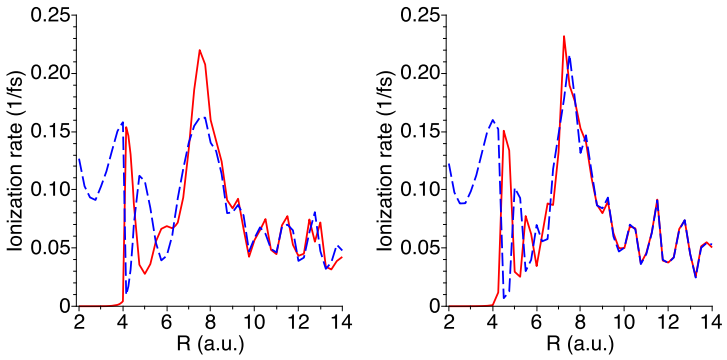

(a) (b)

Figure 3.10: The same as in figure 3.8, but the field parameters are $\omega = 0.02\,au$ (a) $\omega = 0.01\,au$ (b) and $F = 0.07549\,au$.

intensity, the peak structure narrows and moves slightly towards smaller R. For $R > 12$ au the ionization rates for the upper and lower states become competitive. In the large-R limit the rates approach each other, since the two complex eigenvalues become nearly-degenerate.

In figure 3.10 the ionization rates as a function of internuclear separation R are shown for two laser frequencies at the increased field intensity of $I = 2.0 \times 10^{14}\,W cm^{-2}$. The results for the lower and upper states merge for large R as $\omega \to 0$. They do resemble the DC limit for the upper state near $R = 8\,au$ with the AC rate for both states approaching 15% of the DC upper-state value.

In Figure 3.11 we show the ionization rate vs R, but the field parameters are $\lambda = 800\,nm$ and $I = 3.2 \times 10^{14} W\,cm^{-2}$, which means the wavelength is somewhat

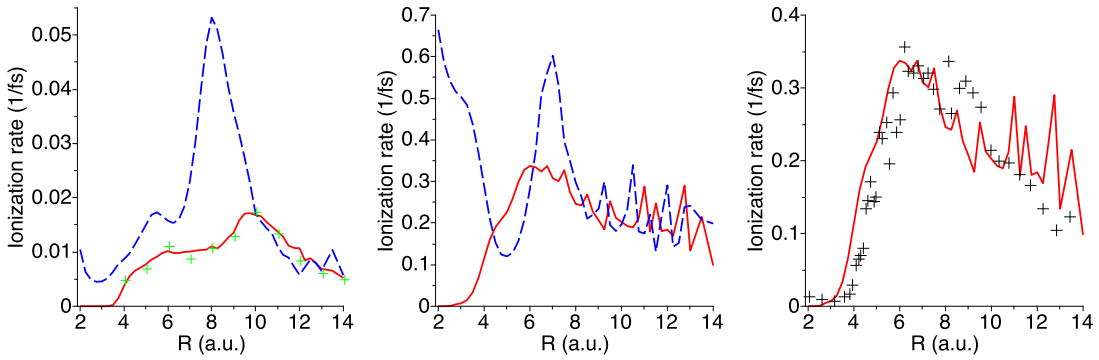

(a) (b) (c)

Figure 3.11: The same as in figure 3.8, but the field parameters are $\omega = 0.05695\,au$ and $F = 0.0533\,au$ (a) $F = 0.095489\,au$ (b, c). (a) green crosses: Bandrauk and Lu [77]. (c) the black crosses are experimental results [5] which have been normalized to our theoretical values; the red curve shows the lower state data from panel (b).

shorter and the intensity is larger than for the previously used values of $\lambda = 1064\,nm$ and $I = 2 \times 10^{14} W\,cm^{-2}$. In both panels (a, b) of Figure 3.11 the ionization rate for the upper state of the ion is much increased, which is due to the fact that the upper state does always stay well above the middle barrier and can be ionized easily. The peak in the ionization rate for the lower state moves towards smaller values of R, because a stronger field distorts the double-well Coulomb potential more deeply. We should note that the increased field strength causes a vanishing of the second peak in the ionization rate for the lower state of the H_2^+ ion. In panel (a) the ionization rate for the lower state is compared with the theoretical value previously

obtained (green crosses) [78]. In panel (b) at larger R the two states are mixed strongly and oscillate. Panel (c) shows a comparison of the lower state results with experimental data obtained by Gibson *et al* [5]. The experimental measurements are normalized to the theoretical calculations since they were recorded as relative data only.

Indeed it is amazing to note that the experimental data and theoretical calculations show together a dominant peak around $R = 6\,au$, and they agree reasonably well with each other. From the previous discussion we know that the first peak can be simply interpreted by the over-the-barrier mechanism. Then as R varies, the lower state shifts up gradually and around $R \approx 3.5\,au$ it rises above the outer barrier of the two-well potential, and around $R \approx 4.75\,au$ it gets caught by the middle barrier of the electronic potential. At the large R calculation does not show a dominating second large peak for the lower state, but shows several sharp structures while mixing with the upper state.

The absence of the second peak is still under discussion and the subject of investigations from both theoretical and experimental points of view. Ben-Itzhak *et al* [9] argued that one reason for the disappearance in reality can be the nuclear motion (non-adiabatic effects), washing out the structure.

Moreover, in the case of field intensity $I = 1.5 \times 10^{15} W\,cm^{-2}$, Gibson *et al* [5] obtained experimental data for the ionization rate for the lower state of the ion,

and theoretical calculations were carried out [53, 79, 80]. The experimental data and theoretical calculations have not shown any sign of the second peak in this case.

3.4 Summary

Floquet calculations in a pseudospectral representation for the lowest two H_2^+ eigenstates are shown to display rather different behaviour in the small-ω limit for the two peak regions in the ionization rate.

For the first peak region ($R \approx 5\,au$) the density plots of the coupled-channel Floquet eigenfunctions demonstrate that while the upper state has remnants of a nodal structure (near $z = 0$), the ionization rates oscillate against each other as a function of R. The oscillation pattern becomes more rapid as $\omega \to 0$.

The outer peak region ($R \approx 9\,au$) shows a different situation. The upper- and lower-state density plots have similar structures in between the nuclei. The inner tunneling barrier causes localized density to oscillate from one nucleus to the other as a function of time. The ionization rates for the upper and lower states become the same in this region.

Finally, we note that for the large-R peak the calculated ionization rates seem to approach an $\omega \to 0$ limit. The rates are approximately $10 - 15\%$ of those found in the DC limit for the upper state in Chapter 2. This should be considered

reasonable, since in the AC case the field is at a strength close to its peak value for about one tenth of the laser cycle.

We tested our findings in a limited range of intensities for which the lower state at equilibrium separation $R = 2\,au$ has a small ionization rate due to the large tunneling barrier. The upper state, however, ionizes quite readily even for $R = 2\,au$ via an over-the-barrier mechanism. Since lasers of higher intensities are becoming available, it will be of interest to extend these calculations to stronger fields to explore the regime where the lower state will also experience strong ionization at small R.

4 High-order harmonic generation for the hydrogen molecular ion in an intense linearly polarized laser field

In this chapter we discuss Floquet calculations of high-harmonic generation (HHG) for the lowest two electronic states of H_2^+ by strong continuous-wave laser fields. The chapter starts with a discussion of the physical mechanism of this phenomenon in Sect 4.1. Sect. 4.2 presents the framework to calculate harmonic generation spectra from the non-Hermitian Floquet approach. Results are presented and discussed in Sect. 4.3. A summary follows in Sect. 4.4.

Originally published as Ts. Tsogbayar and M. Horbatsch, J. Phys. B: At. Mol. Opt. Phys. **47** 115003 (2014).

4.1 Introduction

From both theoretical and experimental points of view, HHG is one of the most studied nonlinear phenomena for atoms and molecules interacting with an intense laser field, in which the system emits radiation at multiples of the laser frequency [81]. The physical mechanism of HHG is well understood for atoms using a three-step model [82, 83, 84] (Figure 4.1): (i) the electron is released by tunnel ionization from the atom core; (ii) the free electron is accelerated by the oscillating laser field, and later is driven back to the core; (iii) the electron can recombine with the core to emit a high-energy photon. This semiclassical formulation for the three-step model is based on the strong-field approximation (SFA) by Lewenstein et al [84].

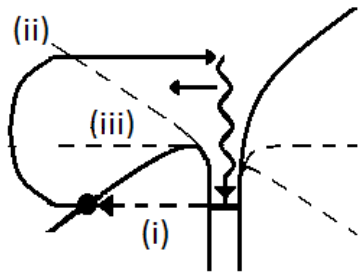

Figure 4.1: Three-step model for the HHG: (i) tunneling ionization; (ii) acceleration of the electron by the oscillating laser field; (iii) recombination with the core to emit a high-energy photon.

In the SFA one considers a direct coupling between the initial bound state and the continuum, i.e., one ignores step-wise excitation via higher bound states.

The model predicts a plateau in the harmonic spectra where many harmonics have similar strength, and it ends with a sharp cutoff. At the cutoff the maximum energy of the returning electron which is released at time $t_{ion} = 0.05\,T$ and collides at $t_{coll} = 0.7\,T$ is well approximated by the simple and universal formula $I_p + \Delta v^2(t)/2 = I_p + 2U_p[\sin(\omega t_{coll}) - \sin(\omega t_{ion})]^2 = I_p + 3.17U_p$, where I_p is the ionization potential of the atom and U_p is the pondermotive potential with F the laser electric field strength and T is a period of laser field, and ω the angular frequency in atomic units, respectively. The velocity of the electron $v(t)$ is obtained as a solution of the equation of motion for a free electron, $\ddot{x} = -F\cos(\omega t)$. The cutoff position can be estimated by

$$N_{max} = (I_p + 3.17U_p)/\omega. \tag{4.1}$$

For symmetric diatomic molecules Kopold et al [85] extended the discussion of this (semi)-classical cutoff formula. They investigated two phenomena, which can become particularly important if one considers dissociating molecules, i.e., systems at large internuclear separation R. The so-called simpleman formula (4.1) is modified, since the ionized electron produced at nucleus A upon re-collision can be re-combining either at nucleus A or B. This can lead to a cutoff that is higher than the atomic one given in Eq. (4.1). In addition, there is the possibility that the field ionizes an electron at atom A, accelerates it, and recombination occurs directly at atom B. These classical cutoff positions have to be taken carefully, since

they ignore the potential role of the Compton profile of the initial state, and the argumentation based on electron localization during ionization and recombination makes sense only at large R, if the molecular orbital nature of the states is taken into account. Nevertheless, Ref.[85] serves to illustrate that the cutoff energies represent stationary points at which enhanced HHG should be observed. Evidence is presented in [85] from quantum calculations in a zero-range model potential for molecular cutoffs higher than Eq.(1), increasing the coefficient from 3.17 by up to a third for the cases considered.

Theoretical investigations for diatomic molecules, such as, the H_2 molecule and the H_2^+ ion were initially carried out by Krause et al [86] and Zuo et al [78, 87]. They performed a direct numerical solution of the TDSE to obtain the HHG spectra. An alternative approach is the Floquet formalism which was employed successfully by Potvliege and Shakeshaft [88] to obtain the HHG spectra for H atoms using Sturmian basis functions. A treatment of HHG for complex atoms in intense laser fields based on R-matrix-Floquet theory has been given by Burke et al [89, 90]. Yet another method for time-periodic systems is the Floquet approach combined with complex rotation of the coordinate [91, 92].

For atomic hydrogen, the hydrogen molecule and molecular ion calculations of HHG spectra within the Floquet method combined with a complex rotated coordinate have been extensively investigated by S-I. Chu and his co-workers [93, 94,

95, 96, 97]. In those works a generalized pseudospectral approach was used for the spatial discretization of the resonant Hamiltonian, and a non-Hermitian split-operator technique was implemented for the time-evolution operator. Telnov and Chu presented benchmark results for HHG for monochromatic intense laser fields for the H_2^+ ion in [96].

In this chapter our goal is to report on HHG spectra for the lowest two states of H_2^+ in a linearly polarized intense laser field (with electric field aligned with the molecular axis), using the Floquet approach combined with a CAP. This methodology was implemented in Chapter 3 to calculate the ionization rates for the lowest two electronic states of the ion by strong continuous laser fields in the low-frequency limit. Given that the ionization rates reported in Chapter 3 vary strongly with R it is of interest to explore HHG, since the first step in the harmonic generation process is ionization. We compare our rates for the R-dependence of HHG with those obtained in [78] and [96]. Our method differs from that of Ref.[96] in that we do not use a time propagator, but assemble the wave function from the Floquet eigenstates.

4.2 Calculation of HHG spectra from the non-Hermitian Floquet approach

Once we have found the time-dependent Floquet wave function $\Psi(\mathbf{r}, t)$ via equation (1.21), we can compute the time-dependent dipole moment along the internuclear axis, $d(t)$, as

$$d(t) = \langle \Psi(\mathbf{r}, t) | z | \Psi(\mathbf{r}, t) \rangle \,. \tag{4.2}$$

Following [96, 98], the nth-order harmonic generation rates Γ_n (the number of photons with frequency $n\omega$ emitted per unit time) are calculated by the Larmor formula

$$\mathbf{\Gamma}_n = \frac{4n^3\omega^3}{3c^3}|d_n|^2, \tag{4.3}$$

where c is the speed of light, and d_n is the Fourier transform of the time-dependent dipole moment (4.2) according to

$$d_n = \frac{1}{T}\int_0^T dt \exp(in\omega t)\, d(t). \tag{4.4}$$

It is common in the literature to either show the rates (4.3) or to show the HHG spectrum as

$$D_n = \log(|d_n|^2). \tag{4.5}$$

which has a stronger fall-off with n.

As shown by Telnov and Chu [96] in Floquet theory the HHG rates are obtained to the same accuracy irrespective of whether one uses the dipole operator (4.2) or the velocity or acceleration forms.

4.3 Results and Discussion

4.3.1 HHG rates for the equilibrium separation $R = 2\,au$

We first attempted to reproduce the HHG spectra previously reported by Telnov and Chu [96]. In our grid representation we have two main parameters, and the results for the harmonic spectra appear to be sensitive to them, implicitly via the Floquet wave function $\Psi(\mu, \nu, t)$. One of two (artificial) parameters which control the wave function is μ_c, which determines the region where the CAP starts. Another one is the absorbing strength parameter η. Ideally, the results ought to be insensitive to these two parameters. It is obvious that the value of μ_c should be larger than the quiver radius of a free electron $\alpha_0 = F/\omega^2$ (in atomic units), because the main contribution to the harmonic generation spectra comes from the free electron driven back to its parent ion or two-centre core. The concern is that strong absorption of outgoing flux may weaken HHG spectra.

In analogy to the η-trajectory in the calculation of the resonance parameter $E_F^{(0)}$ in Chapter 3, we initially obtain the HHG rate Γ_n for varying $\eta^{(0)}$. Within a

certain range of the $\eta^{(0)}$-trajectory, namely where the complex eigenenergy value $E_F^{(0)}$ stabilizes, the resonance wave function is assumed to be accurate, and in turn, it should yield accurate HHG spectra.

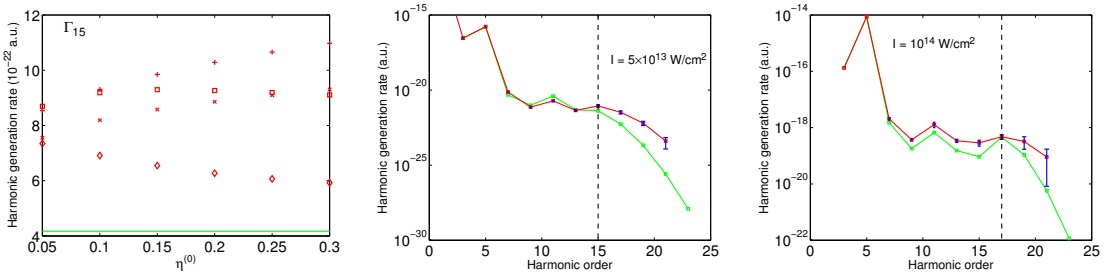

(a) (b) (c)

Figure 4.2: The HHG rate for the lower state of H_2^+ at internuclear separation $R = 2\,au$, and for wavelength $\lambda = 532\,nm$: (a) $I = 5 \times 10^{13}\,W/cm^2$, Γ_{15} rate vs $\eta^{(0)}$ for various values of μ_c, namely 13.5 (diamonds), 14.5 (squares), 15.5 (plus signs) and $16.5\,a.u.$ (crosses); the green line shows the value from Telnov and Chu [96]; (b) plot for more harmonics than shown in (a); here $N_{max} \approx 15$; (c) for intensity $I = 1 \times 10^{14}\,W/cm^2$, for which $N_{max} \approx 17$. The green line in (b, c) connects the theoretical data of [96] while the red line connects the present data. The blue error bars are based on the calculations with different μ_c. The vertical dashed lines indicate the semi-classical cutoff values N_{max}.

In panel (a) of Fig. 4.2 we show the HHG rate Γ_{15} vs $\eta^{(0)}$ for the lower state of the H_2^+ ion at the equilibrium separation ($R = 2\,au$) in a field of intensity

$I = 5 \times 10^{13}\, W/cm^2$ and wavelength $\lambda = 532\, nm$. In panel (a) we show results for Γ_{15} for $\eta^{(0)} \geq 0.05$ (for $\eta^{(0)} \leq 0.05$ the computation is inaccurate). We chose four different μ_c values, in the range $13.5 \leq \mu_c \leq 16.5\, au$, which are much larger than $\alpha_0 = 5.15\, au$. The bottom green line shows the result obtained by Telnov and Chu [96]. Our results for Γ_{15} are higher by up to a factor of 2.5, as compared to the value $\Gamma_{15} = 4.17 \times 10^{-22}\, au$ given in [96]. In panel (b) we show the HHG spectrum. We note that for orders $n < 15$ the agreement with the results of [96] is good and is independent of the chosen value of μ_c. In all plots showing HHG rates we omit results for order $n = 1$, because they are usually much higher. The cutoff position as predicted by Eq.(4.1) is around $n = 15$, which is indeed consistent with our result. For each harmonic order we use four different values of μ_c to compute Γ_n, and use them to define an average value with standard deviation. Panel (c) shows the same plot for the HHG rate for the doubled intensity, $1 \times 10^{14}\, W/cm^2$. The cutoff law is clearly obeyed around $n = 17$ by both the present and previous [96] results. As compared to Ref.[96] our HHG rates are higher above the cutoff but also less certain.

In Fig. 4.3 data are shown for increased laser intensities. In panel (a) of Fig. 4.3 in the HHG spectra the cutoff position moves up to 19, but the calculated spectrum extends the plateau to higher orders. Our result agrees well with that obtained by Telnov and Chu [96]. In panel (b) of Fig. 4.3 we show the same plot for

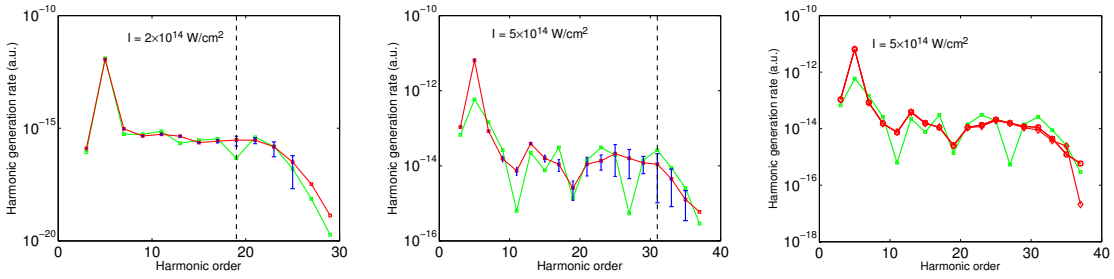

(a) (b) (c)

Figure 4.3: The same plot as shown in Figure 4.2 (b, c), however the laser intensities are $I = 2 \times 10^{14}\, W/cm^2$ (a), and $I = 5 \times 10^{14}\, W/cm^2$ (b). In (c) the same plot is shown as in (b), but the number of Floquet channels is chosen to be $N_F = 72$ (diamonds), 82 (squares) and 86 (circles), respectively. The classical cutoff positions are around 19 (a), and 31 (b, c) and are indicated by vertical dashed lines.

$I = 5 \times 10^{14}\, W/cm^2$. In this case although the general features of the obtained HHG spectrum follow those of Ref.[96], it does show significant deviation at certain harmonic orders, namely for $n = 5, 11$ and 27. To check our answer carefully, we gradually increased the number of Floquet channels, because the HHG rates at higher harmonic orders require a higher number of photon couplings. In panel (c) of Fig. 4.3 we display the same plot as shown in panel (b), but the number of Floquet channels N_F is 72, 82 and 86, respectively. Thus we know that the results are converged at $N_F = 86$ in the HHG order range presented in our plots. The data in Fig. 4.3c are based on a matrix diagonalization with $N_F = 86$, with the specified

truncation imposed in eqn (1.22) when computing (4.2).

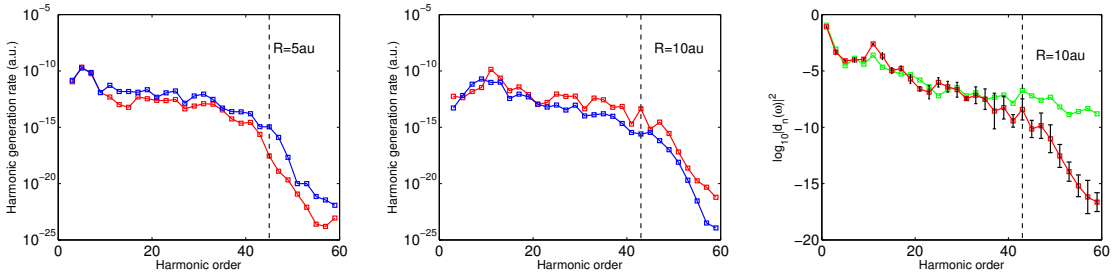

(a) (b) (c)

Figure 4.4: HHG rates for the lower (red) and and upper (blue) states of the H_2^+ ion at $R = 5\,au$ (a) and $R = 10\,au$ (b). Panel (c) shows the HHG spectrum (Eq. (4.5)) for the lower state (red) at $R = 10\,au$ to be compared with the result obtained in [78] (green). The laser field parameters are $F = 0.0533\,au$ and $\omega = 0.0428\,au$.

Next we continue with HHG rates while moving towards the low-frequency limit. In Fig. 4.4 we show the rates for the lower (red) and upper (blue) states for the H_2^+ ion for laser fields of $I = 1 \times 10^{14}\,W/cm^2$ and $\lambda = 1064\,nm$. All HHG calculations are carried out with $\eta^{(0)} = 0.25$. Panel (a) shows the rates at internuclear separation $R = 5\,au$, while panels (b, c) demonstrate corresponding results at $R = 10\,au$. Given that $\omega = 0.0428\,au$, the cutoff positions given by the classical formula (4.1) are found around $n = 45$ and $n = 43$ at $R = 5\,au$ and $R = 10\,au$, respectively, and are shown by vertical dashed lines for the lower state in Figure 4.4 (for the upper state, the cutoff position is close to it, since both states

have almost the same ionization potential at large internuclear separations). As discussed by Bandrauk and co-workers in [78, 87], these classical cutoff positions are referred to as the atomic plateau. They argue that a first plateau region can be identified as a molecular plateau: its cutoff occurs at harmonic order

$$n_M = \frac{2\Omega_R}{\omega} = \frac{2d_0F}{\omega} \approx \frac{RF}{\omega}, \tag{4.6}$$

where Ω_R is the Rabi frequency for driving transitions between the $1\sigma_g$ and $1\sigma_u$ states and the transition dipole moment d_0 grows towards $R/2$ with increasing R (for details cf [78]). According to this model in which the two lowest states are driven resonantly, since $\omega \geq \epsilon_{1\sigma_u} - \epsilon_{1\sigma_g}$, the values of the cutoff positions can be found at $n_M = 5$ for $R = 5\,au$, and $n_M = 11$ for $R = 10\,au$, respectively. These calculated values of n_M can be observed in the data given in Figure 4.4. Panel (c) of Figure 4.4 shows the HHG spectrum calculated by equation (4.4) for the lower state of the ion and its comparison with that obtained in [78] (green). We note that the agreement between the Floquet result and the calculation for a finite 30- cycle pulse is excellent up to order 39. Beyond this order the harmonics for the finite pulse with square envelope continue to be strong, while the Floquet results fall off.

4.3.2 Harmonic generation rates as a function of internuclear separation R

In this subsection we present HG rates for moderate orders n, i.e., in the molecular plateau region at the intensity $1 \times 10^{14}\, W/cm^2$ as a function of internuclear separation R. The ionization rates for the lower and upper states of the ion for two wavelengths of the laser field, $1064\, nm$ and $800\, nm$ are shown in panel (a) of Figs 3.1 and 3.11. Our goal is to demonstrate how the enhancement of the ionization rate in certain R-regions affects the HG rates within the region of the molecular plateau, i.e., for $n \leq n_M$ (4.6).

In Figure 4.6 we show the rates Γ_n as functions of R for the lower (red) and upper (dashed blue) states of the ion using a common linear scale. As can be seen in Fig. 4.6c, when R varies from the equilibrium separation 2 to $12\, au$, the fifth harmonic for the lower and upper states has very similar large peaks around $R \approx 5\, au$, where the first enhancement of the ionization rate (Figure 3.10a) occurs. Note, however that the ionization rate patterns for the two states are not as similar as those of Γ_5. Observing Γ_7 and Γ_9 in panels (d, e) we find a shift in the peaks towards larger R. For the lower state a large peak in the ionization rate appears around $R \approx 9\, au$ (Figure 3.1a), and Γ_9 also displays a peak there (Figure 4.6e). Meanwhile, the upper-state Γ_9 rate deviates for $R > 8\, au$, somewhat in accord with

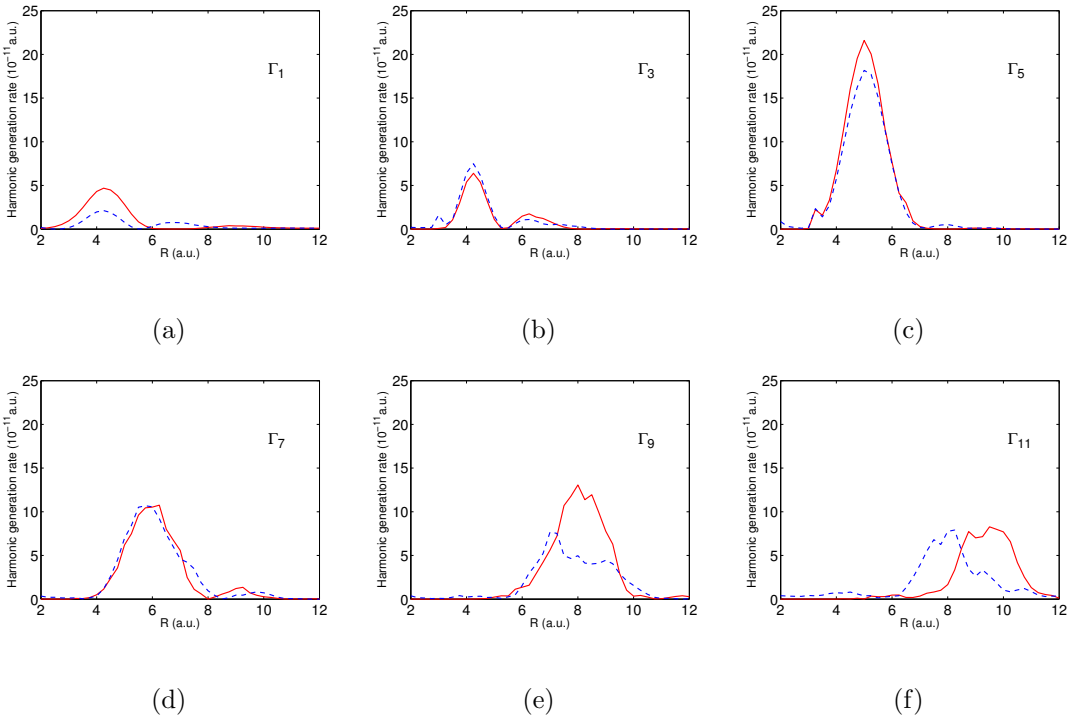

Figure 4.5: Harmonic generation rates as functions of internuclear separation R for the lower (solid red) and upper (dashed blue) states of the H_2^+ ion. The harmonic order is shown on each plot. The laser field parameters are $F = 0.0533\,au$ and $\omega = 0.0428\,au$.

its decrease in ionization rate.

The HG rates for higher orders of n (beyond $n = 11$) become smaller, thus we do not show them here. Together Figures 3.1a and 4.6 demonstrate that the enhancement of the ionization rate for the lower and upper states of the hydrogen molecular ion can be linked to an enhancement of the harmonic generation rates in certain R-ranges. This happens for harmonic orders within the molecular plateau

region $n < n_M$.

As a further demonstration of the correspondence we show the HG rate as function of R for $\lambda = 800\,nm$ in Figure 4.7, while the ionization rates are given in Figure 3.11a. The upper state shows a very prominent ionization peak around $R = 8\,au$.

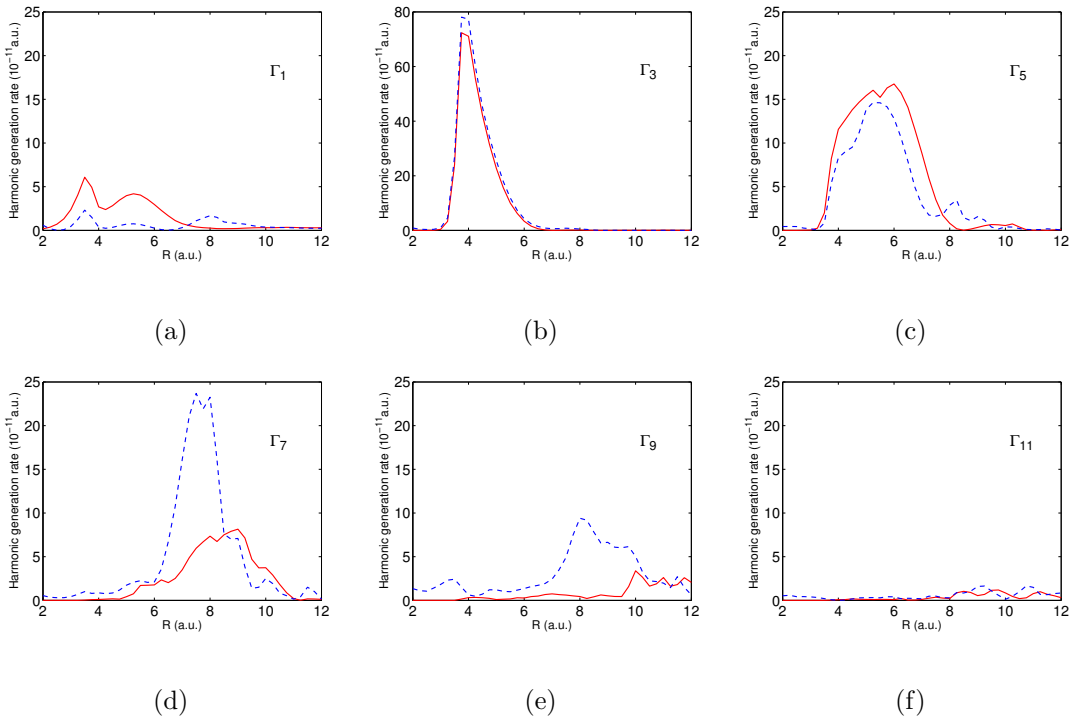

Figure 4.6: The same plots shown as in Figure 4.5, however for $\omega = 0.05695\,au$ and $F = 0.0533\,au$.

As can be observed from Figure 4.6b, Γ_3 displays strong peaks around $R \approx 4\,au$ for both states in a region where the ionization rates are not strong. This is particularly true for the lower state. This behavior, thus, must come from bound-

state populations [78]. However, a major peak can be observed in Γ_7 around $R \approx 8\,au$ (Figure 4.7d) for the upper state, where a strong enhancement of the ionization rate does occur (Figure 3.10a). A significant feature around $R \approx 8\,au$ is also visible in Γ_9 for the upper state (Figure 4.7e).

Compared to the $\lambda = 1064\,nm$ case Fig. 4.7f shows a much weakened Γ_{11} rate. This is a consequence of the molecular cutoff law (4.6). Naively, one might think that a reduced wavelength λ (increased ω) will simply push the cutoff to higher R. However, at $R > 10\,au$ the ionization rates drop (cf. Fig. 3.10a). One reason why the dynamics change at large R is that the upper and lower states become nearly degenerate, i.e., $\omega \gg \epsilon_{1\sigma_u} - \epsilon_{1\sigma_g}$, and the strong-coupling regime [78] is reached.

From the behavior of the $n < n_M$ rates Γ_n shown in Figs. 4.6-7 it is obvious that the dipole moment Eq.(4.2) is a complicated periodic function of time when $R \gg 2\,au$. It is no longer dominated by the fundamental frequency ω, as is usual for atomic HG spectra.

4.4 Summary

We have presented non-Hermitian Floquet calculations of HHG for the lowest two H_2^+ eigenstates in monochromatic strong laser fields using the length gauge. A pseudospectral representation of the Hamiltonian was applied, and the CAP method was used to avoid the calculation of an oscillatory tail in the coupled-channel resonance

wave function. In this approach even though we needed to solve a large non-Hermitian matrix problem to get the solution for the TDSE, we avoided problems that are associated with time-stepping algorithms, particularly the accumulation of phase errors.

The results for the HHG rates for the lower state of H_2^+ in strong laser fields were compared with previous calculations in the literature [78, 96]. The cutoff positions in the HHG spectra were examined and compared with the classical cutoff formula given in [84]. Good agreement was found for $I \leq 10^{14} W/cm^2$ and some deviations were observed at higher intensities for high harmonic orders.

In the region of the molecular plateau, $n < n_M$, (cf. Eq.(4.6)), while considering separations $R = 4 - 10\, au$ it is shown that the enhancement of the ionization rate for the lower and upper states at $R \approx 8\, au$ causes an enhancement of the harmonic generation rate in the following way: Γ_5 for both states and Γ_9 for the lower state of H_2^+ in a field of $I = 10^{14} W/cm^2$ and $\lambda = 1064\, nm$ show peaks; similarly Γ_7 for the upper state of H_2^+ in a field of $I = 10^{14} W/cm^2$ and $\lambda = 800\, nm$ displays peaks at $R_c \approx 8\, au$. The lower bound of this enhanced HG region $R = 4\, au$ is characterized by near-resonant coupling $\omega \approx \epsilon_{1\sigma_u} - \epsilon_{1\sigma_g}$. It is bounded at $R \approx 10\, au$ by the decrease in ionization rate (cf. Fig. 3.1a). On the other hand, for $\lambda = 800\, nm$ Γ_3 dominates the HG spectra around $R \approx 4\, au$ for the upper and lower states, which cannot be associated with an enhanced ionization rate, but with strong resonant

coupling, as explained in Ref.[78].

5 Future outlook

5.1 Summary

In this dissertation we have investigated systematically the DC and AC Stark resonance parameters for the lowest two states of the H_2^+ ion in moderately strong fields.

Previous calculations were based on the complex scaling method, while the present work was performed using a complex absorbing potential. The DC Stark resonance parameters obtained here improve upon previous results. An enhancement of the ionization rate as a function of internuclear distance R for the upper state at so-called critical distances R_c is observed in these calculations and is interpreted by means of the over-the-barrier mechanism using electron density plots.

An enhancement of ionization rates as a function of R for both the lower and upper states of the molecular ion in a low-frequency AC field have been obtained using Floquet theory and compared with literature results. Our results show that this enhancement is independent of the laser wavelength (or frequency) and that

the two states mix strongly as R varies. The interpretation for the enhancement is supported by the appearance of avoided and true crossings of the complex Floquet energy eigenvalues.

The electronic Born-Oppenheimer Hamiltonian depends parametrically on R. Thus, when a true crossing occurs in the real part of the complex-valued Floquet quasi-energy eigenvalue, the imaginary part which yields the ionization rate undergoes an avoided crossing. This structure gives rise to maxima in the ionization rates as a function of R.

Furthermore, harmonic generation rates were calculated for the lower and upper states of the ion and the results were compared with those in the literature. It was shown that the enhancement of the ionization rate at critical internuclear separations has an effect on harmonic generation rates of moderate orders, namely within the molecular plateau region.

A further interest of this work is to apply it to many-electron molecules, the simplest of which is H_2. Dissociation dynamics of the H_2 molecule have been carried out extensively theoretically [99, 100, 101] and experimentally [102, 103, 104].

Based on previous experience we begin with the calculation of the energy eigenvalue for the ground $1\sigma_g^2$ state of the H_2 molecule. The initial approach is to use the self-consistent-field (SCF) method, and then to generalize to the simplest approximation in density-functional theory (DFT), a local density approximation (LDA)

for other molecules, such as N_2 and O_2. In the following section we show some first results for the H_2 molecule.

5.2 Self-consistent field method for the H_2 molecule

For the simplest molecule H_2, consisting of two hydrogen atoms, a solution to the stationary Schrödinger equation can not be found analytically. We shall not discuss the Hartee-Fock or Hartree-Fock-Slater approximation in detail here, but it can be found in [105, 106].

The HF wave function for the ground $1\sigma_g^2$ state of H_2 can be written as

$$\Psi = \frac{1}{\sqrt{2}}\,\psi(1)\psi(2)\,\{\alpha(1)\beta(2) - \alpha(2)\beta(1)\}, \tag{5.1}$$

where α and β are single-electron spin wave functions and $\psi(i)$ are spatial wave functions. The two electron spins form a combined spin-singlet state, which is anti-symmetric under particle exchange.

We first consider the Hartree-Fock equation which for a two-electron spin singlet system is local, since the exchange term cancels one half of the direct Poisson term:

$$[H(\mathbf{r}) + G(\mathbf{r})]\psi(\mathbf{r}) = \epsilon\,\psi(\mathbf{r}) \tag{5.2}$$

where ϵ is orbital energy and the Hamiltonian $H(\mathbf{r})$ is a one-electron Hamiltonian (cf Eq. (1.63)). Since the two electrons are distinguished by their spin we have $\psi(1) = \psi(2) = \psi$, and only the ground state of (5.2) is populated.

The interelectronic Coulomb potential $G(\mathbf{r})$ satisfies the Poisson equation

$$\nabla^2 G(\mathbf{r}) = -4\pi\rho(\mathbf{r}), \tag{5.3}$$

where $\rho(\mathbf{r})$ is the single-electron density, $\rho = |\psi|^2$.

The Hartree-Fock equation (5.2) is solved (self-consistently) iteratively together with the Poisson equation (5.3). Since the Hartree-Fock equation is solved for one electron only, the computational method is almost the same as for H_2^+.

The total energy for the ground $1\sigma_g^2$ state of the hydrogen molecule in the Hartree-Fock approximation can be found as:

$$E^{\mathrm{HF}} = 2\epsilon - \langle V_{ee}\rangle + \frac{1}{R}, \tag{5.4}$$

where $\langle V_{ee}\rangle$ is the electron-electron repulsion interaction given by

$$\langle V_{ee}\rangle = \int\int \frac{\rho(1)\rho(2)}{r_{12}} dv_1 dv_2. \tag{5.5}$$

In Table 5.1 we show some results for the ground state of H_2 obtained in the Hartree-Fock approximation and their comparison with literature values. The convergence criterion in interelectronic potential was set to $\Delta\langle V_{ee}\rangle = 10^{-8}\, au$ and 15 iterations were needed to achieve this criterion.

The Hartree-Fock method does not give the correct dissociation limit at large R, therefore one needs to take into account so-called configuration interaction (CI) to get the correct dissociation limit. The multiconfiguartion SCF method for the H_2 molecule is discussed in [111].

Table 5.1: Summary of the SCF calculation for $1\sigma_g^2$ state of H_2 at $R = 1.40\,au$ and $b = 120\,au$.

N	M	$\epsilon\,(au)$	$\langle V_{ee}\rangle\,(au)$	$E^{\mathrm{HF}}\,(au)$	$\langle r^2\rangle\,(au)$	$\langle Q\rangle\,(au)$
48	12	-0.594 658 585 396	0.658 598 141 163	-1.133 629 597 668	2.573 929 832 565	0.243 288 900 824
56	12	-0.594 658 570 253	0.658 598 145 515	-1.133 629 571 735	2.573 929 832 594	0.243 288 900 824
64	12	-0.594 658 569 993	0.658 598 145 769	-1.133 629 571 469	2.573 929 832 556	0.243 288 900 823
72	12	-0.594 658 569 991	0.658 598 145 756	-1.133 629 571 453	2.573 929 832 556	0.243 288 900 823
Ref. [107]				-1.133 629	2.573 6	0.243 3
Ref. [108]		-0.594 658 567		-1.133 629 57	2.573 930	0.243 2888
Ref. [109]		-0.594 658 5694		-1.133 629 5717		
Ref. [110]		-0.594 658 5687		-1.133 629 571 456		

After implementing the SCF method for the hermitian Hamiltonian of the H_2 molecule we continued with the calculation for the non-hermitian Hamiltonian which describes the DC Stark problem. This problem is solved similarly as the DC problem for H_2^+ discussed in Chapter 2. In Figure 5.1 we show the ionization rate as a function of the field strength F for the ground $1\sigma_g^2$ state of the H_2 molecule at internuclear separation $R = 1.46\,au$ and their comparison with those obtained by Kudrin and Krainov [112] and Saenz [113]. Kudrin and Krainov obtained their results using an analytic formula obtained from a simple Heitler-London wave function (for detail cf [112]). Saenz's result is based on the modified Ammosov-Delone-Krainov (MADK) model which includes a barrier-suppression mechanism [114]. This plot

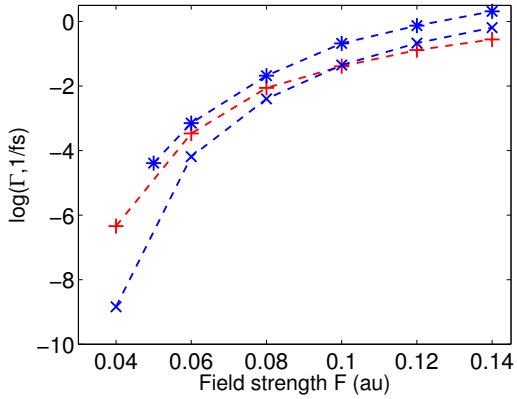

Figure 5.1: Ionization rate as a function of the electric field strength F for the $1\sigma_g^2$ state of the H_2 molecule at $R = 1.46\,au$. Curves: present results (dashed red with plus signs) and literature values (dashed blue with crosses) [112] and (dashed blue with asterisks) [113].

shows that for field strengths $F < 0.06\,au$ the difference between the MADK and SCF results is small compared to analytically obtained values [112], and that all values rise gradually as the electric field strength F increases. For $F \approx 0.1\,au$ our calculated and the analytic rates [112] are comparable, and for stronger fields the difference grows again. Overall, one can say that the differences between different model calculations are large. This is to be expected, because tunneling processes are sensitive to details such as resonance position and barrier heights.

To obtain the ionization rate for the state of the molecule at larger R, one needs to take into account CI, combining at least the ground and first excited states. An

enhancement of the ionization rate for the ground state of H_2 in a strong DC electric field at $R = 6\,au$ has been shown by Saenz [99], in which he used the exact wave functions for the ground and excited states which were obtained originally by Kolos *et al* [107]. The enhancement is associated with a mixing with an excited state which can dissociate into H^+ and H^-. This mixing does not occur, however, in the adiabatic limit.

Bibliography

[1] K. Codling and L. J. Frasinski, *Dissociative ionization of small molecules in intense laser fields*, *J. Phys. B*, **26**, 783, 1993.

[2] A. Giusti-Suzor *et al.*, *Dynamics of H_2^+ in intense laser fields*, *J. Phys. B*, **28**, 309, 1995.

[3] J. H. Posthumus *et al.*, *The dissociation dynamics of diatomic molecules in intense laser fields*, *J. Phys. B*, **29**, L525, 1996.

[4] E. Constant, H. Stapelfeldt and P. B. Corkum, *Observation of Enhanced Ionization of Molecular Ions in Intense Laser Fields*, *Phys. Rev. Lett.*, **76**, 4140, 1996.

[5] G. N. Gibson, M. Li, C. Guo, and J. Neira, *Strong-Field Dissociation and Ionization of H_2^+ Using Ultrashort Laser Pulses*, *Phys. Rev. Lett.*, **79**, 2022, 1997.

[6] H. Stapelfeldt *et al.*, *Time-resolved Coulomb explosion imaging: A method to measure structure and dynamics of molecular nuclear wave packets*, *Phys. Rev. A*, **58**, 426, 1998.

[7] I. D. Williams *et al.*, *Fast-beam study of H_2^+ ions in an intense femtosecond laser field*, *J. Phys. B*, **33**, 2743, 2000.

[8] Th. Ergler *et al.*, *Time-Resolved Imaging and Manipulation of H_2 Fragmentation in Intense Laser Fields*, *Phys. Rev. Lett.*, **95**, 093001, 2005.

[9] I. Ben-Itzhak *et al.*, *Elusive enhanced ionization structure for H_2^+ in intense ultrashort laser pulses*, *Phys. Rev. A*, **78**, 063419, 2008.

[10] T. Zuo and A. D. Bandrauk, *Charge-resonance-enhanced ionization of diatomic molecular ions by intense lasers*, *Phys. Rev. A*, **52**, R2511, 1995.

[11] Z. Mulyukov, M. Pont, and R. Shakeshaft, *Ionization, dissociation, and level shifts of H_2^+ in a strong dc or low-frequency ac field*, *Phys. Rev. A*, **54**, 4299, 1996.

[12] M. Plummer and J. F. McCann, *Field-ionization rates of the hydrogen molecular ion*, *J. Phys. B*, **29**, 4625, 1996.

[13] Xi Chu and Shih-I Chu, *Complex-scaling generalized pseudospectral method for quasienergy resonance states in two-center systems: Application to the Floquet study of charge resonance enhanced multiphoton ionization of molecular ions in intense low-frequency laser fields*, *Phys. Rev. A*, **63**, 013414, 2000.

[14] Roger G. Newton, *Scattering Theory of Waves and Particles*, Dover Publications, Inc., 1982.

[15] John R. Taylor, *Scattering Theory*, Dover Publications, Inc., 2000.

[16] G. Breit and E. Wigner, *Capture of Slow Neutrons*, *Phys. Rev.*, **49**, 519, 1936.

[17] A. J. F. Siegert, *On the Derivation of the Dispersion Formula for Nuclear Reactions*, *Phys. Rev.*, **56**, 750, 1939.

[18] R. A. Bain, J. N. Bardsley, B. R. Junker and C. V. Sukumar, *Complex coordinate studies of resonant electron-atom scattering*, *J. Phys. B*, **7**, 2189, 1974.

[19] R. Santra, and L. S. Cederbaum, *Non-Hermitian electronic theory and applications to clusters*, *Phys. Rep.*, **368**, 1, 2002.

[20] W. P. Reinhardt, *Method of complex coordinates: application to the Stark effect in hydrogen*, *Int. J. Quant. Chem. Symp.*, **10**, 359, 1976.

[21] W. P. Reinhardt, *Complex Coordinates in the Theory of Atomic and Molecular Structure and Dynamics*, *Ann. Rev. Phys. Chem.*, **33**, 223, 1982.

[22] E. Brändas and P. Froelich, *Continuum orbitals, complex scaling problem, and the extended virial theorem*, *Phys. Rev. A*, **16**, 2207, 1977.

[23] S. Graffi, V. Grecchi and B. Simon, *Complete separability of the Stark problem in hydrogen*, *J. Phys. A*, **12**, L193, 1979.

[24] J. Aguilar and J. M. Combes, *A class of analytic perturbations for one-body Schrödinger Hamiltonians*, *Commun. Math. Phys.*, **22**, 269, 1971.

[25] E. Balslev and J. M. Combes, *Spectral Properties of Many-body Schrödinger Operators with Dilatation-analytic Interactions*, *Commun. Math. Phys.*, **22**, 280, 1971.

[26] B. Simon, *Quadratic Form Techniques and the Balslev-Combes Theorem*, *Commun. Math. Phys.*, **27**, 1, 1972.

[27] T. N. Rescigno, C. W. McCurdy, Jr. and A. E. Orel, *Extensions of the complex-coordinate method to the study of resonances in many-electron systems*, *Phys. Rev. A*, **17**, 1931, 1978.

[28] B. R. Junker, *Recent developments in the use of complex scaling in resonance phenomena*, *Adv. Atom. and Mol. Phys.*, **18**, 208, 1982.

[29] Y. K. Ho, *The method of complex coordinate rotation and its applications to atomic collision processes*, *Phys. Rep.*, **99**, 1, 1983.

[30] N. Moiseyev, *Quantum theory of resonances: calculating energies, widths and cross-sections by complex scaling*, *Phys. Rep.*, **302**, 211, 1998.

[31] G. Jolicard and E. Austin, *Optical potential stabilisation method for predicting resonance levels*, *Chem. Phys. Lett.*, **121**, 106, 1985.

[32] U. V. Riss and H. D. Meyer, *Calculation of resonance energies and widths using the complex absorbing potential method*, *J. Phys. B*, **28**, 1475, 1995.

[33] G. Jolicard, C. Leforestier and J. Austin, *Resonance states using the optical potential model. Study of Feshbach resonances and broad shape resonances*, *J. Chem. Phys*, **88**, 1026, 1988.

[34] R. Lefebvre, M. Sindelka and N. Moiseyev, *Resonance positions and lifetimes for flexible complex absorbing potentials*, *Phys. Rev. A*, **72**, 052704, 2005.

[35] R. Santra, *Why complex absorbing potentials work: A discrete-variable-representation perspective*, *Phys. Rev. A*, **74**, 034701, 2006.

[36] E. Ackad and M. Horbatsch, *Supercritical Dirac resonance parameters from extrapolated analytic continuation methods*, *Phys. Rev. A*, **76**, 022503, 2007.

[37] G. Floquet, *Equations differentielles lineares a coefficients periodiques*, *Ann. Ec. Norm. Suppl.*, **12**, 47, 1883.

[38] J. H. Shirley, *Solution of the Schrödinger Equation with a Hamiltonian Periodic in Time*, *Phys. Rev.*, **138**, B979, 1965.

[39] H. Sambe, *Steady States and Quasienergies of a Quantum-Mechanical System in an Oscillating Field*, *Phys. Rev. A*, **7**, 2203, 1973.

[40] David Gottlied and Steven A. Orszag, *Numerical Analysis of Spectral Methods: Theory and Applications*, SIAM, 1977.

[41] D. Funaro, *Polynomial Approximation of Differential Equations*, Springer-Verlag, 1992.

[42] Llyod N. Trefethen, *Spectral Methods in MATLAB*, SIAM, 2000.

[43] John P. Boyd, *Chebyshev and Fourier Spectral Methods*, Dover, 2001.

[44] Jan S. Hesthaven, Sigal Gottlied, and David Gottlied, *Spectral Methods for Time-Dependent Problems*, Cambridge University Press, 2007.

[45] R. Meyer, *Trigonometric interpolation method for one-dimensional quantum-mechanical problems*, *J. Chem. Phys.*, **52**, 2053, 1969.

[46] C. Clay Marston and Gabriel G. Balint-Kurti, *The Fourier grid Hamiltonian method for bound state eigenvalues and eigenvectors*, *J. Chem. Phys.*, **91**, 3571, 1989.

[47] E. Fattal, R. Baer and R. Kosloff, *Phase space approach for optimizing grid representations: The mapped Fourier method*, *Phys. Rev. E*, **53**, 1217, 1996.

[48] E. Ackad and M. Horbatsch, *Numerical solution of the Dirac equation by a mapped Fourier grid method*, *J. Phys. A*, **38**, 3157, 2005.

[49] J. P. Boyd, C. Rangan, P. H. Bucksbaum, *Pseudospectral methods on a semi-infinite interval with application to the hydrogen atom: a comparison of the mapped Fourier-sine method with Laguerre series and rational Chebyshev expansions*, *J. Comp. Phys.*, **188**, 56, 2003.

[50] E. A. Hylleraas, *On the electronic terms of the hydrogen molecule*, *Z. Physik*, **71**, 739, 1931.

[51] G. Jaffé, *Zur Theorie des Wasserstoffmolekulions*, *Z. Physik*, **87**, 535, 1934.

[52] W. G. Baber and H. R. Hassé, *The two centre problem in wave mechanics*, *Proc. Camb. Phil. Soc.*, **31**, 564, 1935.

[53] Liang-You Peng *et al.*, *A discrete time-dependent method for metastable atoms and molecules in intense fields*, *J. Chem. Phys.*, **120**, 10046, 2004.

[54] L. V. Keldysh, *Ionization in the Field of a Strong Electromagnetic Wave*, *Zh. Eksp. Teor. Fiz.*, **47**, 1945, 1964.

[55] J. H. Posthumus *et al.*, *Dissociative ionization of molecules in intense laser fields: a method of predicting ion kinetic energies and appearance intensities*, *J. Phys. B*, **28**, L349, 1995.

[56] A. D. Bandrauk and H.Z. Lu, *Enhanced ionization of the molecular ion H_2^+ in intense laser and static magnetic fields*, *Phys. Rev. A*, **62**, 053406, 2000.

[57] P. H. Bucksbaum, A. Zavriyev, H. G. Muller, and D. W. Schumacher, *Softening of the H_2^+ Molecular Bond in Intense Laser Fields*, *Phys. Rev. Lett.*, **64**, 1883, 1990.

[58] Ts. Tsogbayar and M. Horbatsch, *Calculation of Resonance Parameters for Atomic Hydrogen in a Static Electric Field*, *Few-Body Syst*, **54**, 431, 2013.

[59] Ts. Tsogbayar, *Static dipole polarizability for the $1s\sigma$ electronic state of the H_2^+ molecular ion*, *J. Phys. B*, **42**, 165007, 2009.

[60] A. Staudte *et al.*, *Attosecond Strobing of Two-Surface Population Dynamics in Dissociating H_2^+*, *Phys. Rev. Lett.*, **98**, 073003, 2007.

[61] T. D. G. Walsh, L. Strach and S. L. Chin, *Above-threshold dissociation in the long-wavelength limit*, *J. Phys. B*, **31**, 4853, 1998.

[62] L. Benassi and V. Grecchi, *Resonances in the Stark effect and strongly asymptotic approximants*, *J. Phys. B*, **13**, 911, 1980.

[63] Y. Huang and Shih-I, *A stationary treatment of time-dependent Hamiltonian by the many-mode floquet formalism and its application to the study of effects of laser pulses in multiphoton processes*, *Chem. Phys. Lett.*, **225**, 46, 1994.

[64] O. Smirnova *et al*, *High harmonic interferometry of multi-electron dynamics in molecules*, *Nature*, **460**, 972, 2009.

[65] M. Ivanov, T. Seideman, P. Corkum, F. Ilkov and P. Dietrich, *Explosive ionization of molecules in intense laser fields*, *Phys. Rev. A*, **54**, 1541, 1995.

[66] S. Chelkowski and A. D. Bandrauk, *Two-step Coulomb explosions of diatoms in intense laser fields*, *J. Phys. B*, **28**, L723, 1995.

[67] A. Giusti-Suzor and F. H. Mies, *Vibrational trapping and suppression of dissociation in intense laser fields*, *Phys. Rev. Lett.*, **68**, 3869, 1992.

[68] C. Trump *et al.*, *Pulse-width and isotope effects in femtosecond-pulse strong-field dissociation of H_2^+ and D_2^+*, *Phys. Rev. A*, **62**, 063402, 2008.

[69] D. Pavičić, A. Kiess, T. W. Hänsch, and H. Figger, *Intense-Laser-Field Ionization of the Hydrogen Molecular Ions H_2^+ and D_2^+ at Critical Internuclear Distances*, *Phys. Rev. Lett.*, **94**, 163002, 2005.

[70] T. Seideman, M. Yu. Ivanov and P. B. Corkum, *Role of Electron Localization in Intense-Field Molecular Ionization*, *Phys. Rev. Lett.*, **75**, 2819, 1995.

[71] R. Shakeshaft and R. M. Potvliege, *Approximate theory for multiphoton ionization of an atom by an intense field*, *Phys. Rev. A*, **36**, 5478, 1987.

[72] L. B. Madsen and M. Plummer, *H_2^+ in intense laser fields: mechanisms for enhanced ionization in the multiphoton regime*, *J. Phys. B*, **31**, 87, 1998.

[73] V. Kokoouline, O. Dulieu, R. Kosloff and F. Masnou-Seeuws, *Mapped Fourier methods for long-range molecules: Application to perturbations in the $Rb_2(0_u^+)$ photoassociation spectrum*, *J. Chem. Phys.*, **110**, 9865, 1999.

[74] L. Tao, C. W. McCurdy, and T. N. Rescigno, *Grid-based methods for diatomic quantum scattering problems. II. Time-dependent treatment of single- and two-photon ionization of H_2^+*, *Phys. Rev. A*, **80**, 013402, 2009.

[75] X. Guan, E. B. Secor, K. Bartschat and B. I. Schneider, *Multiphoton ionization of H_2^+ in xuv laser pulses*, *Phys. Rev. A*, **84**, 033420, 2011.

[76] X. Guan, R. C. DuToit and K. Bartschat, *Photoionization of the H_2^+ ion by ultrashort elliptically polarized laser pulses*, *Phys. Rev. A*, **87**, 053410, 2013.

[77] A. D. Bandrauk and H. Lu, *Generalized space translation and new numerical methods for time-dependent Schroedinger equations of molecules in intense laser fields*, *Journal of Molecular Structure (Theorchem)*, **547**, 97, 2001.

[78] T. Zuo, S. Chelkowski, and A. D. Bandrauk, *Photon-emission spectra of the H_2^+ molecular ion in an intense laser field*, *Phys. Rev. A*, **49**, 3943, 1993.

[79] Liang-You Peng *et el*, *Dynamic tunnelling ionization of H_2^+ in intense fields*, *J. Phys. B*, **36**, L295, 2003.

[80] H. Sabzyan and M. Vafaee, *Intensity dependence of the H_2^+ ionization rates in Ti:sapphire laser fields above the Coulomb-expolsion threshold*, *Phys. Rev. A*, **71**, 063404, 2005.

[81] B. Piraux *et at*, editor, *Proceedings of the Workshop, Super Intense Laser-Atom Physics (SILAP)*, volume 3, 1993.

[82] K. C. Kulander, K. J. Schafer and L. J. Krause, *in Proceedings of the Workshop, Super Intense Laser-Atom Physics (SILAP) III*, in B. Piraux *et at* [81], page 95.

[83] P. B. Corkum, *Plasma perspective on strong field multiphoton ionization*, *Phys. Rev. Lett.*, **71**, 1994, 1993.

[84] M. Lewenstein, Ph. Balcou, M. Yu. Ivanov, A. L'Huillier and P. .B. Corkum, *Theory of high-harmonic generation by low-frequency laser fields*, *Phys. Rev. A*, **49**, 2117, 1994.

[85] R. Kopold, W. Becker, and M. Kleber, *Model calculations of high-harmonic generation in molecular ions*, *Phys. Rev. A*, **58**, 4022, 1998.

[86] L. J. Krause, K. J. Schafer and K. C. Kulander, *Optical harmonic generation in atomic and molecular hydrogen*, *Chem. Phys. Lett.*, **178**, 573, 1991.

[87] T. Zuo, S. Chelkowski, and A. D. Bandrauk, *Harmonic generation by the H_2^+ molecular ion in intense laser fields*, *Phys. Rev. A*, **48**, 3837, 1993.

[88] R. M. Potvliege and R. Shakeshaft, *Multiphoton processes in an intense laser field: Harmonic generation and total ionization rates for atomic hydrogen*, *Phys. Rev. A*, **40**, 3061, 1989.

[89] P. G. Burke, P. Francken, and C. J. Joachain, *R-Matrix-Floquet Theory of Multiphoton Processes*, *EuroPhys. Lett.*, **13**, 617, 1990.

[90] P. G. Burke, P. Francken, and C. J. Joachain, *R-Matrix-Floquet Theory of Multiphoton Processes*, *J. Phys. B*, **24**, 761, 1991.

[91] N. Ben-Tal, N. Moiseyev, C. Leforestier and R. Kosloff, *Positions, lifetimes, and partial widths of metastable quasienergy states by solving the time−dependent complex−scaled Schrödinger equation*, *J. Chem. Phys.*, **94**, 7311, 1991.

[92] N. Ben-Tal, N. Moiseyev, R. Kosloff and C. Cerjan, *Harmonic generation in ionizing systems by the time-dependent complex coordinate Floquet method*, *J. Phys. B*, **26**, 1445, 1993.

[93] D. A. Telnov, J. Wang and S. I. Chu, *Two-color phase control of high-order harmonic generation in intense laser fields*, *Phys. Rev. A*, **52**, 3988, 1995.

[94] X. M. Tong and S. I. Chu, *Theoretical intense study of multiple high-order harmonic generation by ultrashort pulsed laser fields: A new generalized pseudospectral time-dependent method*, *Chem. Phys.*, **217**, 119, 1996.

[95] X. Chu and S. I. Chu, *Self-interaction-free time-dependent density-functional theory for molecular processes in strong fields:? High-order harmonic generation of H_2 in intense laser fields*, *Phys. Rev. A*, **63**, 023411, 2001.

[96] D. A. Telnov, and S. I. Chu, *Ab initio study of high-order harmonic generation of H_2^+ in intense laser fields: Time-dependent non-Hermitian Floquet approach*, *Phys. Rev. A*, **71**, 013408, 2005.

[97] D. A. Telnov, and S. I. Chu, *Ab initio study of the orientation effects in multiphoton ionization and high-order harmonic generation from the ground and excited electronic states of H_2^+*, *Phys. Rev. A*, **76**, 043412, 2007.

[98] L. D. Landau and E. .M. Lifshitz, *The classical theory of fields*, Pergamon-Oxford, 1975.

[99] A. Saenz, *Enhanced ionization of molecular hydrogen in very strong fields*, *Phys. Rev. A*, **61**, 051402(R), 2000.

[100] K. Harumiya, H. Kono, Y. Fujimura, I. Kawata, and A. D. Bandrauk, *Intense laser-field ionization of H_2 enhanced by two-electron dynamics*, *Phys. Rev. A*, **66**, 043403, 2002.

[101] Xi Chu, *Time-dependent density-functional-theory calculation of strong-field ionization rates of H_2*, *Phys. Rev. A*, **82**, 023407, 2010.

[102] S. L. Chin, Y. Liang, J. E. Decker, F. A. Ilkov and M. V. Ammosov, *Tunnel ionization of diatomic molecules by an intense CO_2 laser*, *J. Phys. B*, **25**, L249, 1992.

[103] F. A. Ilkov, T. D. G. Walsh, S. Turgeon, and S. L. Chin, *Dissociative tunnel ionization of H_2 in an intense mid-ir laser field*, *Phys. Rev. A*, **51**, R2695, 1994.

[104] A. Rudenko, B. Feuerstein, K. Zrost, V. L. B. de Jesus, T. Ergler, C. Dimopoulou, C. D. Schröter, R. Moshammer and J. Ullrich, *Fragmentation dynamics of molecular hydrogen in strong ultrashort laser pulses*, *J. Phys. B*, **38**, 487, 2005.

[105] C. Slater, *Quantum Theory of Molecules and Solids, Vol 4, The Self-Consistent Field for Molecules and Solids*, McGraw-Hill, New-York, 1974.

[106] R. G. Parr and W. Yang , *Density-Functional Theory of Atoms and Molecules*, Oxford, 1989.

[107] W. Kolos and C. C. J. Roothaan, *Accurate Electronic Wave Functions for the H_2 Molecule*, *Rev. Mod. Phys.*, **32**, 219, 1960.

[108] L. Laaksonen, P. Pyykkö, and D. Sundholm, *Two-Dimensional Fully Numerical Solutions of Molecular Schrodinger Equations. II. Solution of the Poisson Equation and Results for Singlet States of H_2 and HeH^+*, *Int. Jour. Quan. Chem.*, **23**, 319, 1983.

[109] D. Heinemann, B. Fricke, and D. Kolb, *Solution of the Hartree-Fock-Slater equations for diatomic molecules by the finite-element method*, *Phys. Rev. A*, **38**, 4994, 1988.

[110] A. V. Mitin, *Exact solution of the Hartree-Fock equation for the H_2 molecule in the linear-combination-of-atomic-orbitals approximation*, *Phys. Rev. A*, **62**, 010501(R), 2000.

[111] J. D. Bowman, Jr., J. O. Hirschfelder and A. C. Wahl, *Extended HartreeFock Calculations for the Ground State and HartreeFock Calculations for the First Excited State of H_2*, *J. Chem. Phys.*, **53**, 2743, 1970.

[112] A. A. Kudrin and V. P. Krainov, *Tunneling ionization of a Hydrogen Molecule*, *Laser Physics*, **13**, 1024, 2003.

[113] A. Saenz, *Behavior of molecular hydrogen exposed to strong dc, ac, or low-frequency laser fields. II. Comparison of ab initio and Ammosov-Delone-Krainov rates*, *Phys. Rev. A*, **66**, 063408, 2002.

[114] V. P. Krainov, *Ionization rates and energy and angular distributions at the barrier-suppression ionization of complex atoms and atomic ions*, *J. Opt. Soc. Am. B*, **14**, 425, 1997.